Quantitative Reservoir Characterization of Ommelanden Formation for CO2 Storage Assessment

Abstract:

This research provides an evaluation of the Ommelanden Formation (Upper Cretaceous chalk) and general CCS applications. Based on the core description and analyses (sedimentology of cores, petrophysical properties, thin sections petrography, and micro-CT) of the Ommelanden Formation interval in two wells (Harlingen Field, the Netherlands), the study aims to define the reservoir characteristics in a quantitative approach and evaluate its potential for storing CO2. We determined the reservoir facies by studying the core lithology, sediment structures, and inferred depositional conditions provided by the description of the sedimentary core and thin sections. We interpret the Ommelanden Formation facies as bioturbated chalk with varying degrees of bioturbation and stylolites. It is characterized by medium- to high bioturbation enhancing heterogeneity in the formation. The study found that the intensity of burrowing is associated with stylolites formation. Petrophysical analysis defines porosity, permeability, and the ability of fluids to flow through reservoirs, which are important in determining the reservoir's suitability. Plug porosity measurements range from 11% to 33% of HRL_02 and HRL_04, while cement-reduced porosity estimates from thin sections of both wells are between 1% and 6%. TinyPerm measures 100–120 mD in HRL_02's less fractured zone and 180–200 mD in the fractured zone. By using micro-CT imaging, we can see the pore networks and rock fabrics in great detail. This shows how the main stylolites, which are laterally extended and opened, will be moving fluids through the chalk matrix. All these techniques are integrated to provide a systemic analysis of the reservoir heterogeneity and to help assess the attendant dynamic behavior. Based on the petrophysical properties and fractures observed in this study, we determined four optimal injection zones for CO2 injection. The most suitable intervals for HRL_02 are 1060.4 m to 1062.4 m and 1073.9 m to 1082.4 m. The most optimal zones in HRL_04 are 1038 m to 1052 m and 1052 m to 1056 m. These outcomes are useful for the decision process, including CCS site selection. This research improves our understanding of the future use of chalk reservoirs for sustainable CCS applications.

Earth Sciences MSc thesis project proposal

Name: Abdulrahman Ibrahim Alwadhakhi

First supervisor: Prof. Fadi Henri Nader

Second supervisor: Dr. Fred Beekman

Table of Contents:

1. Introduction

1.1 Climate Change and CO_2 Emissions

Since 1990, the five IPCC assessment cycles have shown an abundance of unprecedented evidence of a fast change in the climate system due to CO_2 emissions. All key climate system components, including the atmosphere, land, cryosphere, biosphere, and ocean, have shown long-term changes (AR6, IPCC, 2021). The prevention of carbon emissions is a very necessary step to prevent global warming and ensure a sustainable environment, which can be achieved through carbon capture and storage (CCS). One of the alerting observations has been the rapidly increasing carbon dioxide levels in the Earth's atmosphere, which reached 418 ppm as of August 31, 2023, for example, according to the Keeling Curve data of 2023. There appears to be an exponential increase in CO_2 concentration since 1960 (Fig. 1). The earth's average temperature has risen by 0.95 °C to 1.2 °C, compared to an increase of only 0.1 °C in the years between 1890 and 1900 (AR6, IPCC, 2021). Carbon emissions primarily contribute to the increase in surface temperature. To fulfill the global commitment according to the Paris Agreement, which came into force in 2016 as a collective effort by 196 parties, carbon emissions should be reduced substantially, as part of attempts to limit climate change to below 2 °C or preferably 1.5 °C before industrial levels. One pivotal way to achieve such reduction and elimination of existing carbon emissions is through carbon capture and storage (CCS) in the subsurface in depleted hydrocarbon reservoirs or deep saline aquifers.

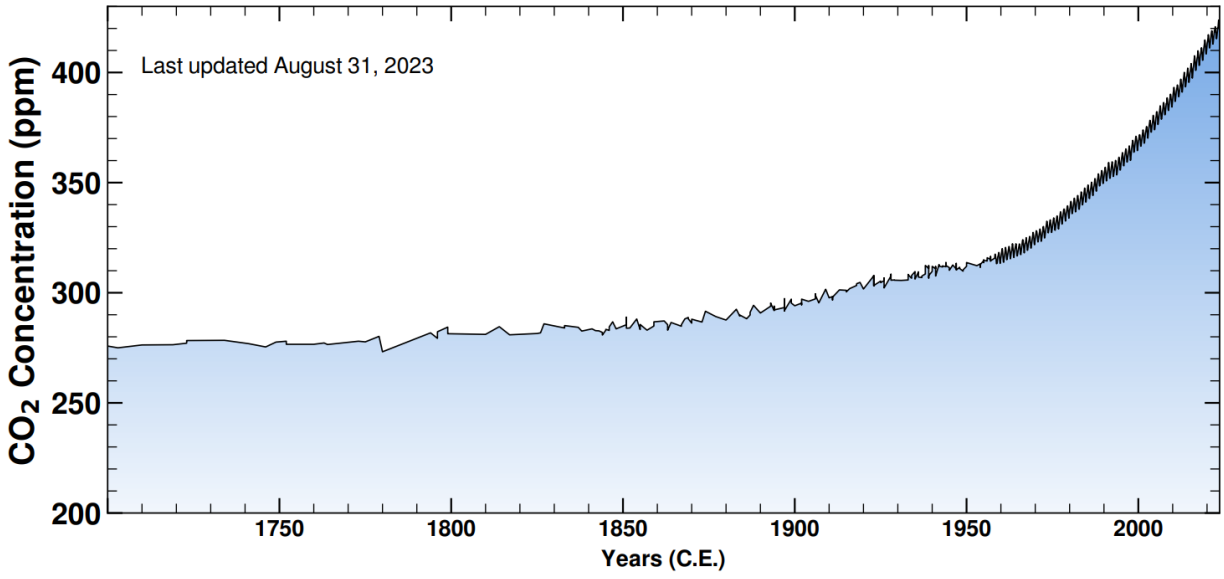

Figure 1: The curve of CO_2 concentrations (in ppm) in the Earth's atmosphere from 1700 to 2023 (Keeling et al., 2001).

1.2 Importance of Carbon Capture and Storage (CCS) in Chalk Reservoirs

Exploration potential for CCS projects in Chalk reservoirs/aquifers is rising in northern Europe, in neighboring countries to the Netherlands, like Denmark, Germany, and England (Bonto et al., 2023). Targets include both depleted hydrocarbon reservoirs and aquifers. Chalk (depleted) hydrocarbon reservoirs in Denmark alone account for 99% of the estimated total available storage capacity (Fig. 2) (ca. 6.19 Gt to 17.42 Gt) (Christensen and Holloway, 2004; Christensen and Larsen, 2004; Vangkilde-Petersen, 2009a). The abundance of chalk rock formations (including aquifers and hydrocarbon reservoirs) extends beyond the North Sea borders and into worldwide locations (Fig. 3), making such rocks significant targets for CCS in various countries. Chalk is a carbonate rock that is known to have low permeability and to be somehow reactive. Therefore, understanding the potentially associated fracture fluid flow and fluid/rock interactions becomes critical before utilizing the chalk as a reservoir for carbon storage both offshore and onshore in depleted hydrocarbon reservoirs and (saline) aquifers.

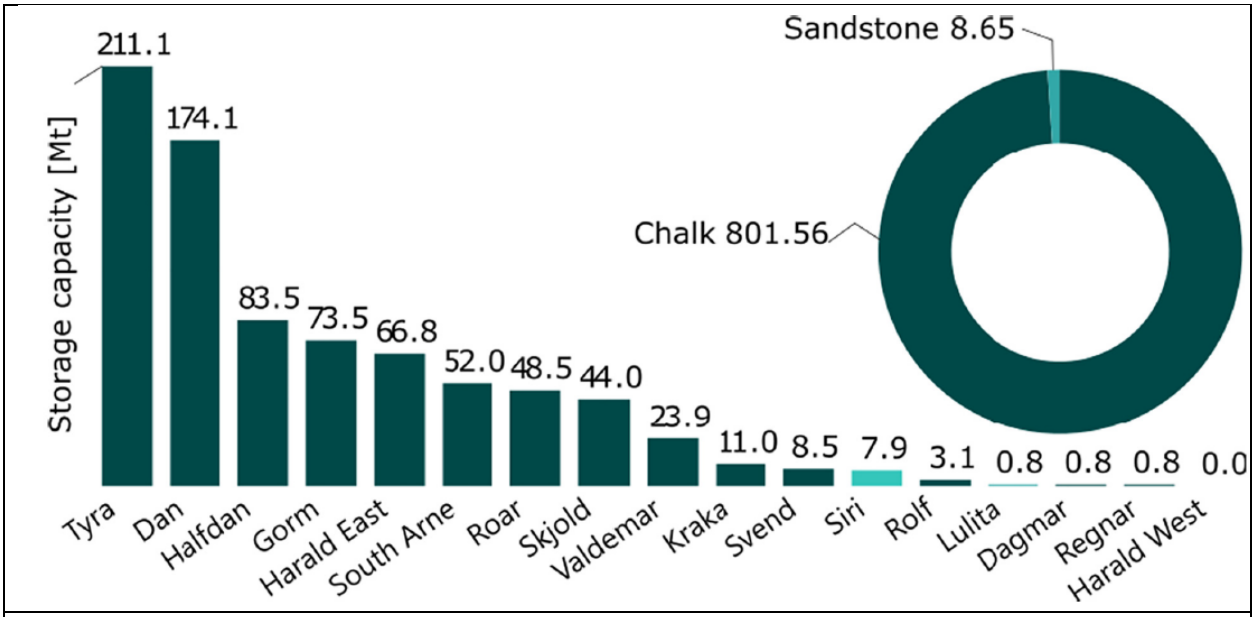

Figure 2: Storage capacity (in Mt) for different fields in the Danish North Sea. Retrieved from (Bonto et al, 2023).

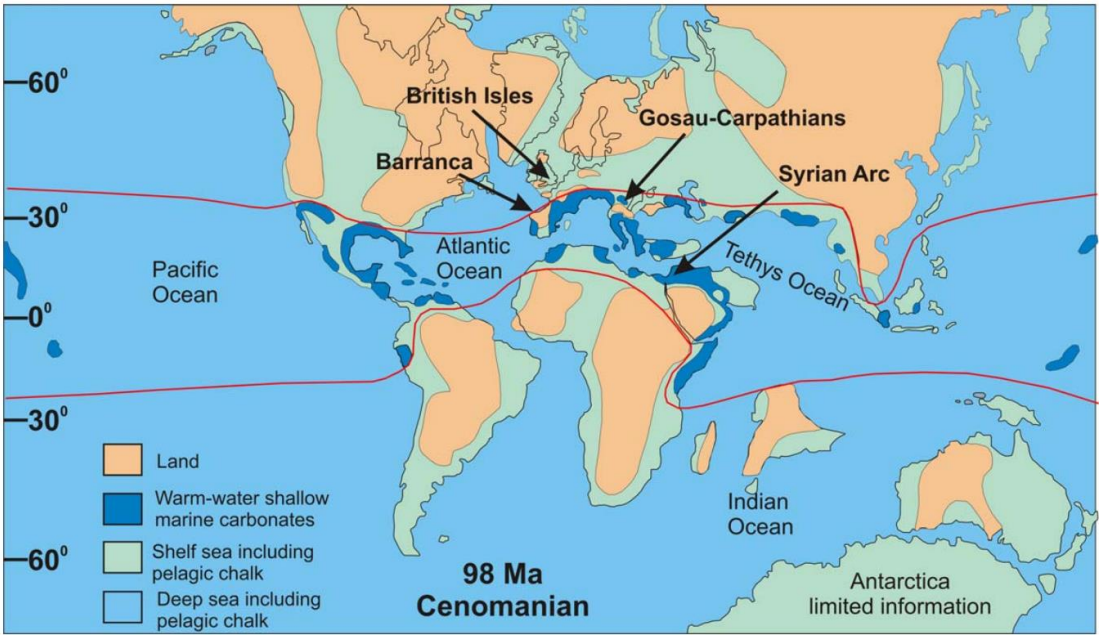

Figure 3: World map at the start of upper Cretaceous showing the position of continents and the ocean and highlighting the abundance of chalk deposits. Map from Morimore (2011).

1.3 Objective and Scope of the Study

Several studies have linked chalk reactivity with CO2, depending on the chalk's different characteristics, such as mineralogical and petrophysical properties (Bonto et al., 2023). Still, the quantitative petrographic and petrophysical characterization of the chalk in terms of its genetic and diagenetic characteristics, including fractures, as well as the impact of CO2-fluid/rock interactions, has not been well studied, particularly for chalk aquifers/reservoirs in the Netherlands. This study will focus on the Ommelanden Formation in the Chalk Group in the Harlingen Upper Cretaceous gas field (Fig. 4), where sufficient subsurface data are available. We analyzed the available 2D seismic lines across the field to provide context for the investigated wells and rock samples. There are nine wells drilled in the field, of which two have core data, Harlingen-02 and Harlingen-04, as well as other petrophysical logs. This project will assess the suitability of the Ommelanden Formation for CO2 storage in the Harlingen Upper Cretaceous gas field (Fig. 4). This assessment will be done by understanding its mineralogy, petrophysical properties, and heterogeneity in the field, as well as the aquifer/reservoir flow properties and the reactivity with carbon dioxide in terms of injectivity (near-well zone) and connectivity (within the aquifer/reservoir zone).

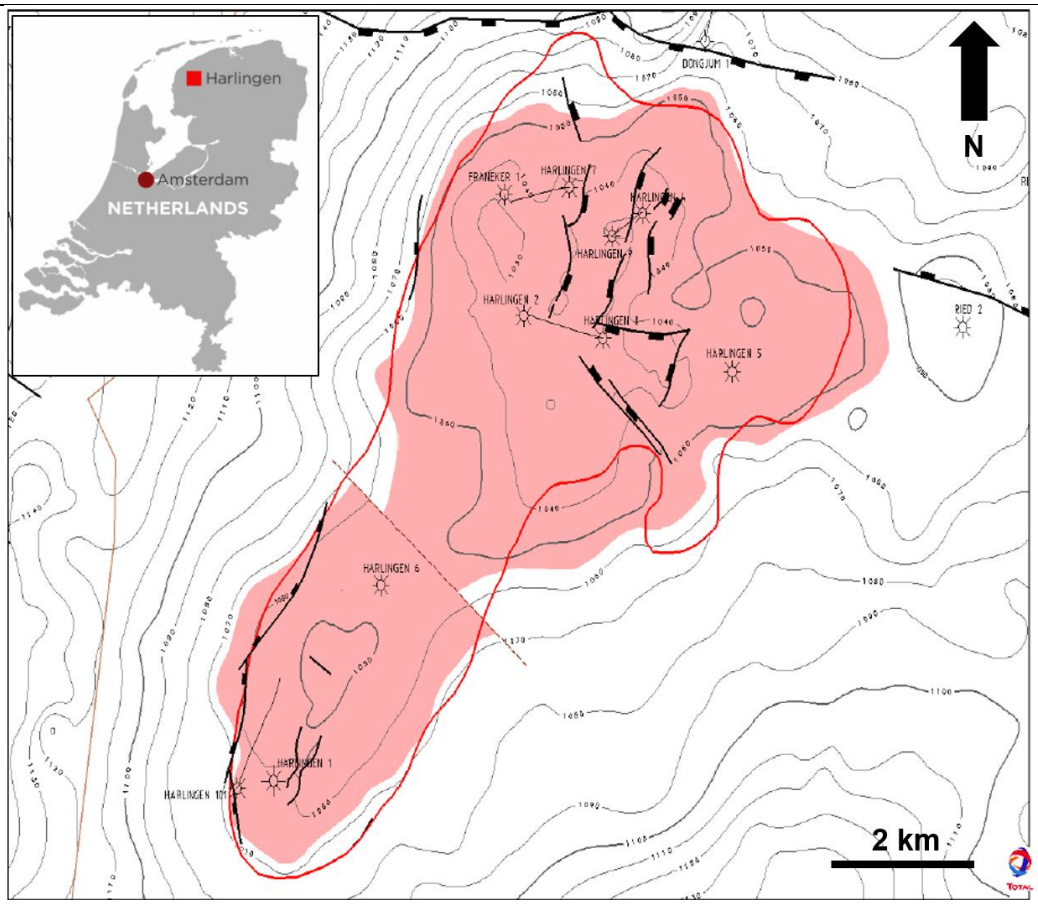

Figure 4: Structural Map of Harlingen Upper Cretaceous Field that is located in the Friesland province, northern Netherlands (index map). The stars represent the wells. Faults are highlighted by black lines. Maps from NLOG website.

2. Geologic Background

2.1 The Harlingen Field Structure and Location

Vermilion Energy Netherlands B.V. discovered and developed the Harlingen Upper Cretaceous Gas Field in 1965. Gas production started in 1988 and shut down by 2008, with 1.77 x 109 m3 of cumulative gas recovery. The field has been shut down due to subsidence in the area, which is around 24.6 cm (Houtenbos, 2010 (subsidence document)). The two wells HRL-02, and HRL-04 were drilled by Petroland B.V. for appraisal of hydrocarbon potential in 1965 and 1984, respectively. The cores of HRL-02 and HRL-04 were described and sampled in the Zeist TNO Core Repository.

The Harlingen Upper Cretaceous Gas Field is a structurally gentle dip anticline located onshore in the Friesland province (Fig. 4). The structure is on the southern edge of the Vlieland basin, and southwest of it lies the Texel IJsselmeer High (Fig. 5), which is among various lows and highs that are typical characteristics of the Dutch North Sea Late Jurassic to Early Cretaceous sedimentary pile. The current structure of Harlingen Upper Cretaceous Gas Field is influenced by two inversion periods in the Vlieland Basin, one in the Late Cretaceous and, the second in the Oligocene to Middle Miocene, which gently folded the structure (Van den Bosch, 1983).

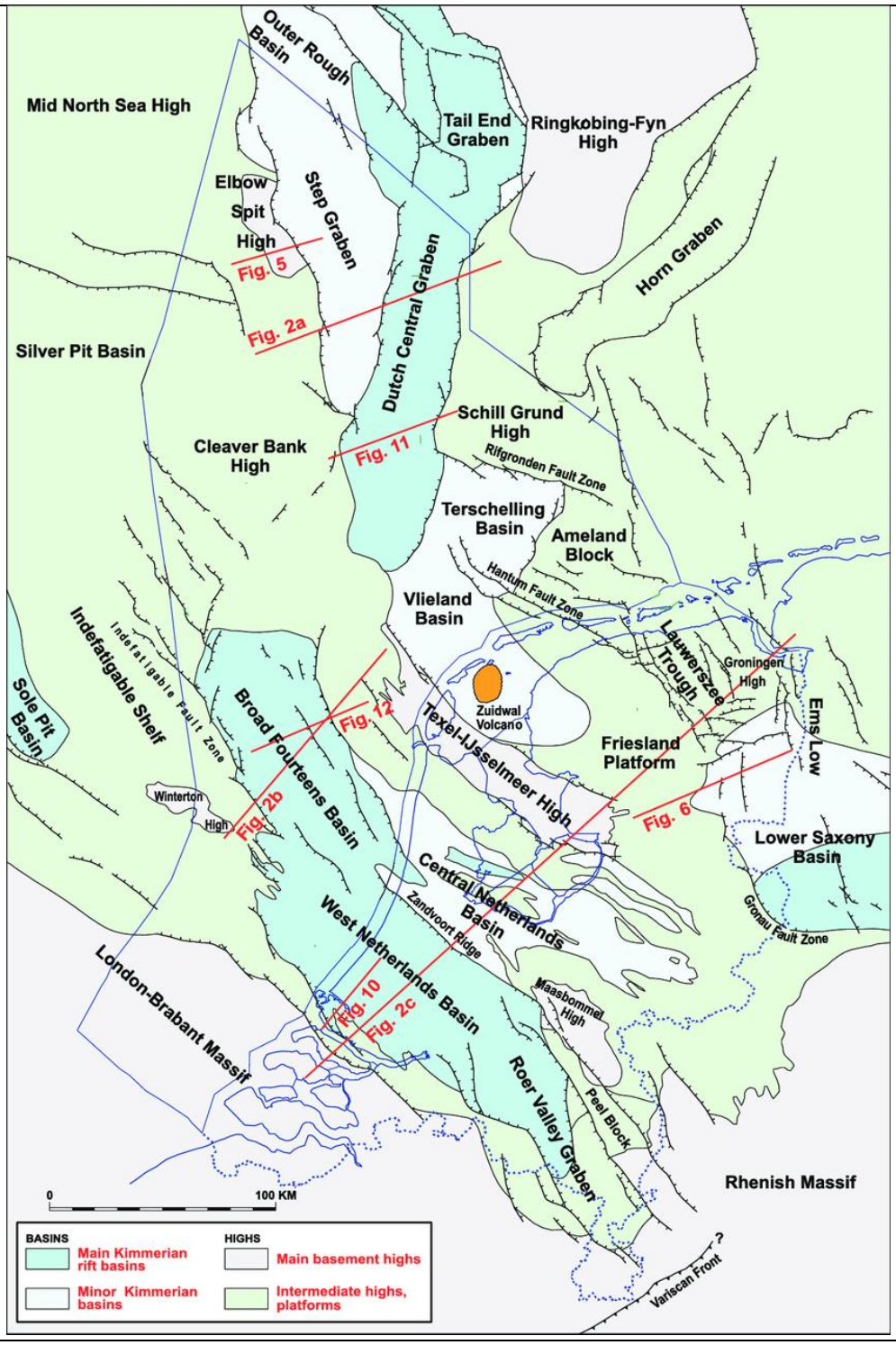

Figure 5: Structural elements map of the Netherlands showing Mid and Late Kimmerian (Jurassic and Early Cretaceous) basins, highs, and platforms. Map from (de jager, 2007).

2.2 The Harlingen Field Stratigraphy

The stratigraphy at Harlingen Field (Fig. 6) from oldest to youngest comprises Westphalian coal-bearing clastics, middle Permian Upper Rotliegend Group clastics, and roughly 900 m of Upper Permian Zechstein Group evaporites overlain conformably by less than 200 m of Lower Triassic clastics (Van den Bosch, 1983). Deformation by tectonics and salt movement started in the Jurassic or earlier in the Triassic, eroding sediments in the Middle and Late Triassic, resulting in the overlain lacustrine and lagoonal Late Jurassic to Early Cretaceous unconformity of the Upper Delfland Formation (Van den Bosch, 1983). The clastic marine of Vlieland Sandstone cuts the Upper Delfland Formation with an angular unconformity. Overlaid by an organic-matter-rich Vlieland Shale of Hauterivian to early Aptian age, the Holland Formation marls of Aptian to Albian age unconformably sit on top of the Vlieland Shales (Van den Bosch, 1983).

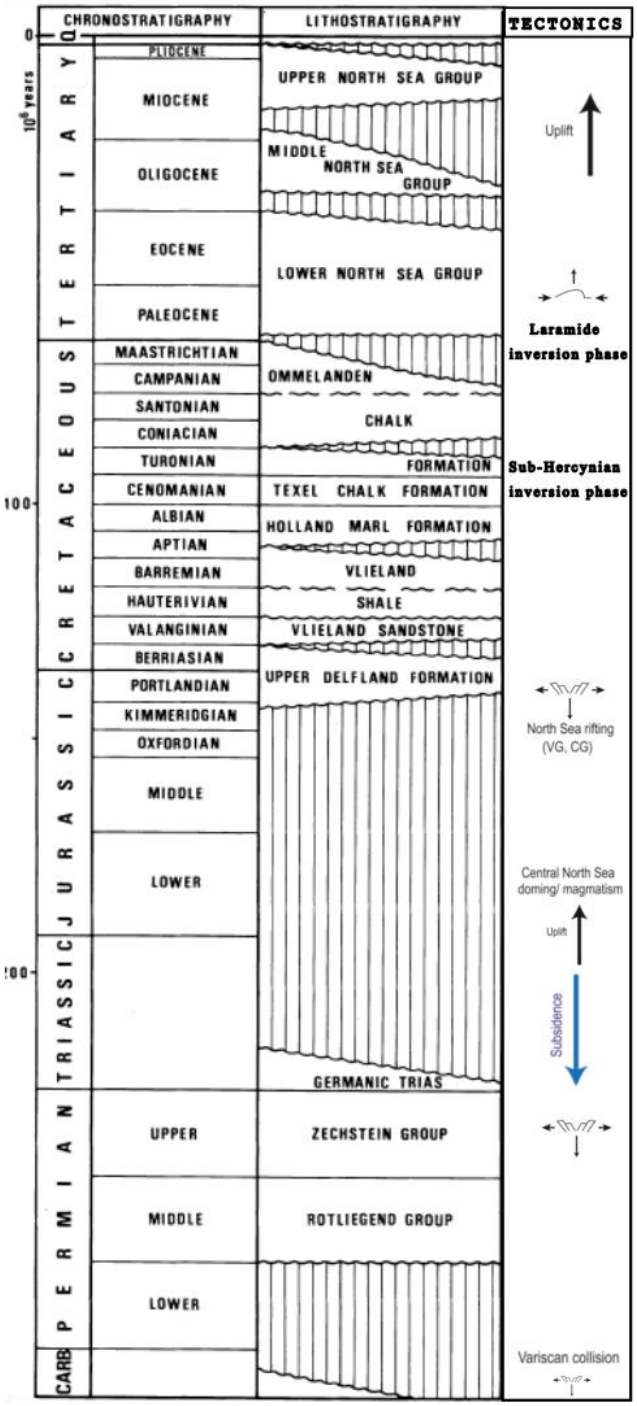

Figure 6: The litho- and chrono-stratigraphy chart of Harlingen. Modified after Van den Bosch (1983) and De Jager (2003).

The Cenomanian argillaceous carbonates of the Texel Chalk Formation were deposited after the Vieland Shales (Van den Bosch, 1983). The subsequent deposition of Ommelanden Chalk was accompanied by the start of basin inversion, which created a local angular unconformity at the beginning of the Coniacian. Basin inversion continued throughout the Late Cretaceous, only locally eroding the Maastrichtian Ommelanden (De Jager, 2003). The uplift and erosion caused by the basin inversion in Harlingen are less than in other areas in the central and southern parts of the Netherlands (Van den Bosch, 1983). The presence of chert nodules and hardground chalk is usually an indication of the two unconformities. Locally, in the Santonian age, a concentration of Chert is present, likely because of erosion and tectonic activity, overlaid by Landen Formation shales of the Paleocene age (Van den Bosch, 1983). The Dongen Formation of the Eocene age is deposited on top of the Landen Formation. An angular unconformity develops at the base of the overlain Middle Oligocene to Early Miocene Middle North Sea Group and lastly, the deposition of the Upper North Sea Group from Middle Miocene until the present time (Van den Bosch, 1983).

2.3 North Sea Chalk

The Chalk group was deposited during a warm climate, and a global rise in sea level, with high organic production accumulating over a period of 40 million years, from 100 Ma to 61 Ma (van der Molen, 2004). An enormous surge of magma "superplume" in mid-Cretaceous times elevates the oceanic crust, causing the sea level to rise (Hays & Pitman, 1973; Larson, 1991a; 1991b). The increase in surface temperature results from a four-fold increase in CO2 levels in the atmosphere, leading to global warming (Huber et al., 2002). The deposition of chalk ended in the early Tertiary by Alpine convergence and mountain building, which is associated with major erosion and the influx of siliciclastic sediments into the oceans and seas, increasing water turbidity (Ziegler, 1990).

North Sea Chalk primarily consists of coccolithophorids, which live in an open marine environment, and an insignificant amount of clay (van der Molen, 2004). Primary depositional structures include bioturbation traces, extensive reworking, and diverse benthic foraminifera (McKinney & Hageman, 2006). Reports indicate that chalk deposition occurs at depths ranging from hundreds to a thousand meters in the center of the basin. The main sedimentation occurs as a suspension in the seawater due to coccoliths' density, which settles at the seabed by the pelagic process (Esmerode & Surlyk, 2009; Fig. 7). The allochthonous chalk is often tectonically enforced by redeposition or by slumps, turbidites, or debris flow (Watts et al., 1980).

In general, low Mg calcite (<5% Mg content; Cloud, 1962) characterizes the chalk commonly found in the geological record (Goldsmith, Graf & Joensuu, 1955). This is because low Mg calcite is more stable at ordinary temperatures and pressures than high Mg calcite and aragonite (Friedman, 1964). The chalk's composition has not been low Mg calcite as a product of diagenesis but rather since the time of its deposition (Hancock, 1975). Clay flasers, which are found within the chalk, are frequently observed at low angles, and associated with fractures. This is interpreted to be due to a post-deposition pressure-solution compaction process that dissolves carbonate and leaves the clay (non-dissolved matter), with the latter being further remobilized in fractures (Hancock, 1975).

The chalk subdivision group in the Netherlands is deposited from Cenomanian to Danian stages in three formations: the Texel Formation, the Ommelanden Formation, and the Ekofisk Formation (Fig. 8). The Texel Formation is equivalent to the Hidra Formation in Norway and Chalk 1 in Denmark. Ommelanden is subdivided into two formations in Norway: the Tor Formation and Hod Formation. On the other hand, Denmark's equivalent formations are numbered Chalk-2 to Chalk-5. Van Wingerden (2016) investigated the sedimentology of different chalk formations and concluded that Ommelanden is one of the most prospective formations due to fracturing and higher permeability (de Jager, 2007)

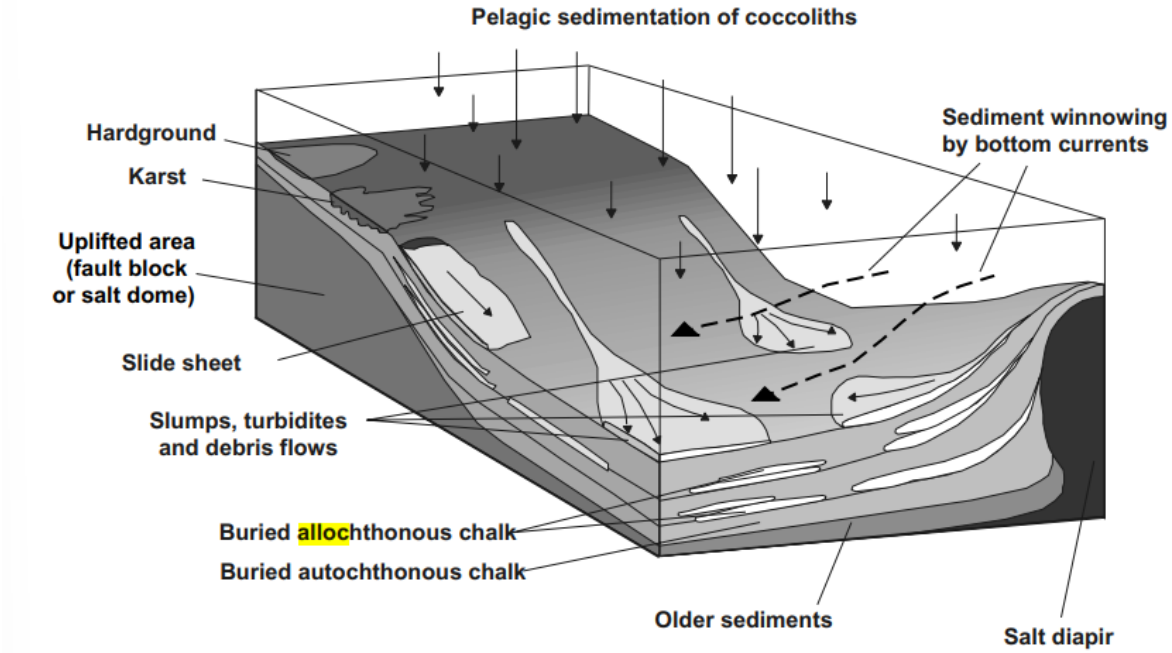

Figure 7: A schematic illustration showing the different depositional environments and associated processes for the chalk distribution. After van der Molen (2004).

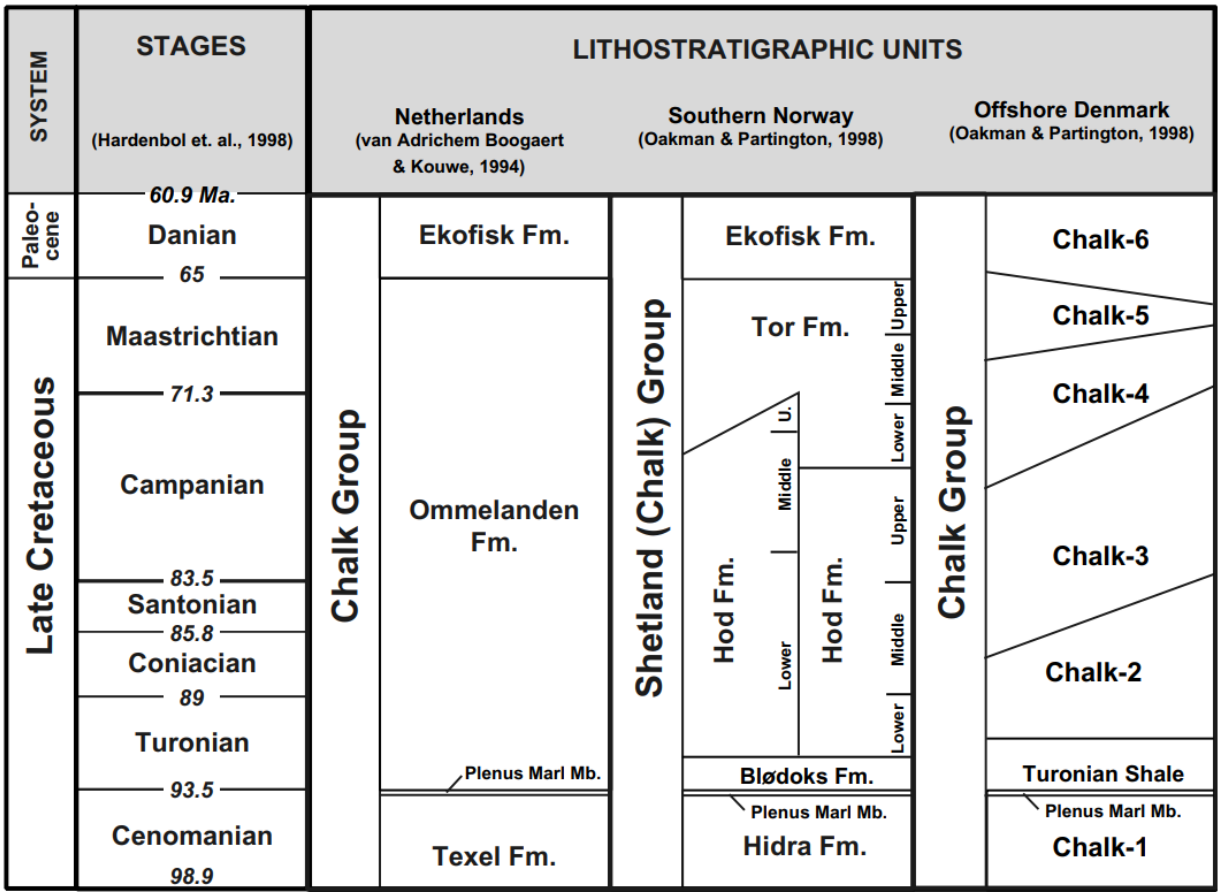

Figure 8: The subdivision of lithostratigraphic Chalk Group in the Danish, Norwegian and the Netherlands sectors of the North Sea (Van der Molen, 2004).

3. CO_2 Storage Capacity and Trapping mechanisms

Determining a geological reservoir's potential to store CO2 is a complex and multifaceted procedure, usually hampered by the scale of investigations and the level of uncertainty (Bachu, 2008). Evaluations of underground (geological) storage capacity have indeed a wide range of degrees of uncertainty (Bachu, 2008). To create useful assessments, large datasets from several disciplines must be combined and tailored to the various assessment levels (Bradshaw et al., 2007). The best-practice method for estimating storage capacity at the local scale involves building a geological model that is based on quantitative characterization of the sedimentary and diagenetic facies and then applying reservoir simulations to predict the dynamics of the model and estimate the foreseen storage potential. These analyses require an enormous amount of data, time, and resources (Bradshaw et al., 2007).

CO2 storage capacity and assessment are complex due to the various trapping mechanisms, which include structural and stratigraphic trapping, mineral trapping, dissolution, residual gas, coal adsorption, and hydrodynamic trapping (Bradshaw et al., 2007; Table 1). Three mechanisms of trapping CO2 in chalk are further described below (i.e., solution, capillary, and mineral trapping mechanisms).

Table 1 – Characteristics of physical and chemical trapping mechanisms

Trapping mechanism	Characteristics							
	Nature of trapping	Effective time frame	Areal size	Occurrence in basin	Issues	Capacity limitation/benefits	Potential size	Capacity estimation method/ requirements
Structural and stratigraphic	Bouyancy trapping within anticline, fold, fault block, pinch-out. CO_2 remains as a fluid below physical trap (seal)	Immediate	10 to 100 s km	Dependent on basins tectonic evolution. Hundreds of small traps to single large traps per basin	Faults may be sealed or open on stress regime, fault orientation and faults could be leak/ spill points or compartmentalize trap	If closed hydraulic system then limited by compression of fluid (few %) in reservoir. If open hydraulic system will displace formation fluid.	Significant	Simple volume calculation of available pore space in trap, allowing for factors that inhibit access to all the trap, e.g. sweep efficiency, residual water saturation
Residual gas	CO_2 fills interestices between pores of the grains of the rocks	Immediate to thousands of years	Basin scale, e.g. 1000 s km	Along migration pathway of CO_2	Will have to displace water in pores. Dependent on CO_2 sweeping through reservoir to trap large volumes	Can equal 15–20% of reservoir volume. Eventually dissolves into formation water	Very large	Requires rock property data and reservoir simulation
Dissolution	CO_2 migrates through reservoir beneath seal and eventually dissolves into formation fluid	100 to 1000 s of years if migrating more than 1000 s of years if gas cap in structural trap and longer if reservoir is thin and has low permeability	Basin scale, e.g. 10,000 s km	Along migration pathway of CO_2 both up dip and down dip	Dependent on rate of migration (faster better) and contact with unsaturated water and pre-existing water chemistry (less saline water better). Rate of migrations depends on dip, pressure, injection rate, permeability, fractures, etc.	Once dissolved, CO_2 saturated water may migrate towards the basin center thus giving the very large capacity. The limitation is contact between CO_2 and water and having highly permeable (vertical) and thick reservoirs	Very large	Requires reservoi simulation and need to know CO_2 supply ratio and injection rate
Mineral precipitation	CO_2 reacts with existing rock to form new stable minerals	10 to 1000 s of years	Basin scale, e.g. 10,000 s km	Along migration pathway of CO_2	Dependent on presence of reactive minerals and formation water chemistry. Could precipitate or dissolve	Rate of reaction slow. Precipitation could ' clog' up pore throats readucing injectivity. Approaches 'permanent' trapping	Significant	Requires rock mineralogy
Hydrodynamic	CO_2 migrates through reservoir beneath seal, moving with or against the regional ground water flow system whist other physical and chemical trapping mechanisms operate on the CO_2	Immediate	Basin scale, e.g. 10,000 km	Along migration pathway of CO_2 with or against the direction of the flow system that may move at rates of cm per year	Dependent on CO_2 migration after the injection period, being so slow that it will not reach the edges of the sedimentary basin where leakage could occur	No physical trap may exist and thus totally reliant on slow transport mechanism and chemical processes. Can include all other trapping mechanisms along the migration pathway	Very large	Requires reservoir simulation and regional reservoir flow model
Coal adsorption	CO_2 preferentially adsorbs onto coal surface	Immediate	10 to 100 s km	Limited to extent of thick coal seams in basins that are relatively shallow	Coals can swell reducing injectivity. Difficult to predict permeability trends. CO_2 adsorption not 100% effective which raises issue of leakage if no physical seal is present	Injectivity poor due to low permeability. Effective at shallower depths than porous sedimentary rocks, but not at deeper depths due to permeability issues. Many injection wells required. If methane liberated might not be net GHG mitigation	Low	Requires gas sorption data and knowledge of permeability trends and coal ' reactivity' to CO_2

Note the different time frames and range of issues. Most mechanisms will operate alongside each other in each trap type. Oil and gas fields predominantly occur in structural and stratigraphic trapping mechanisms.

Table 1: Description of the different CO_2 trapping mechanisms and their characteristics. Table from (Bradshaw et al., 2007).

3.1 Solution Trapping

The injected CO_2 will dissolve gradually in the formation water. Its dissolution depends on pressure, temperature, pH, and electrolyte type (Liu et al., 2011). The solubility of CO_2 decreases with temperature, and salinity but increases with pressure (Bonto et al., 2021). Furthermore, when CO_2 dissolves, the pH decreases, which eventually impacts the solubility of CO_2 in the formation over

prolonged periods. The density of water increases when the CO_2 dissolves, leading to its sinking, below the unsaturated water, which will rise, causing a convection rather than a diffusive type of mixing (Ennis-King and Paterson, 2002, 2005). Ghoshal et al. (2017) estimated that the convective flow in carbonate formations is 50% lower than in other less reactive systems due to calcite's higher reaction rates with CO2 than other minerals. Fractures in some chalk formations, however, may increase the total (vertical) permeability and make it easier for density-driven convective fingers to form, assuming that gravity is stronger than the CO_2 plume. The presence of residual oil in depleted chalk fields will cause the solubility of CO_2 to be faster, compared to injection in “clean” water (Stewart et al., 2017).

3.2 Capillary Trapping

Up to 95% of the injected CO2 can be trapped as residual gas in the micro-pores of the chalk reservoir (Krevor et al., 2015). The risk of leakage is reduced because the gas cannot migrate and is immobile. The higher the water saturation, the higher the efficiency of capillary trapping (Akbarabadi and Piri, 2015). One contentious issue is the possibility of capillary entrapment in carbonate deposits versus clastics. According to data from core flooding tests, carbonates have a lower residual CO_2 saturation than sandstones, depending on wettability and heterogeneity variations (Akbarabadi and Piri, 2015). Nevertheless, carbonate reservoirs may have higher capillary trapping than quartz-rich reservoirs, according to Wang and Tokunaga's (2015) residual gas measurements and capillary pressure-saturation curves on limestone and dolomite cores.

3.3 Mineral Trapping

The chalk will start to dissolve after the pH decreases due to the CO_2 solution in the water. Calcite will precipitate once the evolved fluid/water is locally oversaturated with calcite. This is possible because the dissolved carbonate minerals in the chalk reservoir move freely. High clay content and silicates may inhibit calcite dissolution (Zuddas and Mucci, 1994). Researchers believe that sandstones exhibit higher mineral trapping than carbonates (Rosenbauer et al., 2005). The following chemical reactions describe the mineral trapping in chalk:

First, a weak carbonic acid H_2CO_3 is created when CO_2(g) is dissolved in water CO_2 (aq).

$$CO_2\ (aq) + H_2O = [H_2CO_3] = H^+ + HCO_3^-$$

Since one of the common ions, carbonate CO_3^{2-}, is converted to bicarbonate HCO_3^- in acidic environments, there is an increased dissolution of chalk, $CaCO_3$(s).

$$CO_3^{2-} + H^+ = HCO_3^-$$

Therefore, the reaction between $CaCO_3$(s) and CO_2 (aq) is:

$$CaCO_3(s) + CO_2\ (aq) + H_2O = Ca^{2+} + 2\ HCO_3^-$$

Then there is reprecipitation of calcite, once the solution is oversaturated with calcite (Mineral trapping):

$$Ca^{2+}(aq) + HCO_3^-(aq) = CaCO_3(s) + CO_2(g) + H_2O(l)$$

4. Experimental and numerical approaches to investigate CCS in chalk

4.1 Experimental Methods (Core Flooding Experiments)

Yu et al. (2023) demonstrated experimentally that calcite precipitation can sequester a considerable amount of CO2. Yu et al. (2023) exposed the chalk samples to CO2-saturated water for 37 days at 15 MPa pressure and 50 °C temperature, resulting in a pH drop from 9.44 to 6.5. The specific surface area of the samples increased whereas porosity, pore size distribution, and permeability decreased due to calcite precipitation.

In the North Sea, a supercritical CO2 injection study was conducted on chalk samples from the South Arne Field, proving that CO2 can be stored by both physical trapping and dissolution, which results in an increase in porosity by 2-3% and a slight increase in permeability (Alam et al., 2014). Mechanical weakening was observed on high carbonate content in the pure chalk Tor formation compared to no mechanical weakening in the Ekofisk formation, which has a higher than 12% non-carbonate content.

A significant amount of CO2 can be stored through dissolution and, at the same time, mineral trapping in localized areas. This was demonstrated by a core flooding experiment on a chalk core sample from the Middle East replicating reservoir conditions in that region undergoing injection of CO2-saturated brine in reservoir conditions. The experiments showed an increase in permeability at the inlet due to calcite dissolution and a decrease in permeability at the outlet (Khather et al., 2020). At both the inlet and outlet, the porosity and pore size are observed to decrease due to compaction, which may affect injectivity at the wellbore location (Khather et al., 2020). Olsen (2010,2011) conducted several CO2 core flooding experiments on chalk samples and reported minor effects on porosity and permeability, suggesting long-term stability of storage. The results of the study showed that CO2 can be sequestered primarily by solubility and localized mineral trapping. A decrease in permeability due to the interaction between chalk and CO2 in a core flooding experiment has been reported by yang et al. (2018). Given all these somehow contradictory results, more research is required to better characterize the chalk's heterogeneous properties and to determine whether injecting CO2 into chalk and carbonates is feasible.4.2 Geomechanical Modelling for CO2 Storage

Four CCS clastic reservoirs were examined to be simulated geomechanically to asses for flow dynamics in the reservoir (Orlic, 2016), which showed that many gas reservoirs, which are bounded by sealing faults, one to a few kilometers apart, prevail limited pressure changes (to the gas-bearing fault blocks). The associated induced stress changes affect the gas reservoir and extend 1 to 3 km away into the surrounding rock (Orlic, 2016). Proven seal quality, field data availability, lack of evidence of seal integrity failure due to fault reactivation from seismically active producing Dutch gas fields, and the possible benefits of likely returning the virgin formation pressure and stress state to geomechanical stability are all arguments in favor of storing CO2 in depleted gas fields (Hettema et al., 2002). The simulated results were then compared with actual ground geomechanical observations. It was established that the model predicted high accuracy of ground geomechanical behavior in terms of reservoir pressure and regional stresses.

5. Data & Methodology

5.1 Database

The construction of a database that included well information, well logs, seismic data, core data, and other field reports was the first building block of this project. We retrieved various data types and information from the Dutch Oil and Gas Portal (NLOG). Logs including gamma ray, density, sonic, neutron, induction, and porosity were key inputs for analysis, and they were essential to determining core sampling points. Petrel 2021 software (SLB) was used to visualize and interpret seismic sections. The Petrel software is a platform utilized for the petroleum industry's exploration and production for various data visualization, interpretation, and modeling. The well logs were visualized and analyzed by EasyTrace (Beicip-Franlab, IFPEN, 2021 version) which is a multidisciplinary 1D data processing and editing program that offers a wide range of features for geologists, geophysicists, and reservoir engineers under a very productive package. The core description, acquired air permeability, density plug, permeability plug, and porosity plug were all manually added to the EasyTrace database for a comprehensive analysis and correlation with the well logs and the different data categories.

5.2 Sedimentology and in-situ permeability measurements

The Harlingen Upper Cretaceous Gas Field has two cored intervals covering the Ommelanden chalk reservoir in wells HRL-02 and HRL-04. For wells HRL-02 and HRL-04, the total depth of the described core interval is 15 m and 11 m, respectively. We studied the lithology, fractures, hardness, and mineral compositions of the two cores in Zeist TNO's core repository. Permeability measurements were achieved with the TinyPerm 3 device (New England Research, UK) in-situ on only the HRL_02 core because the HRL_04 core was too fragile, and a firm surface was needed to take reliable permeability measurements. 20 measurements were acquired from the core of HRL_02 (approximately every 1 m, along the accessible cores).

5.3 Petrography

Twelve representative samples were selected from HRL_02, and HRL_04 cores, and corresponding thin sections were prepared at the Thin Section Lab (TSL, France), representing relatively higher porosity and permeability rock intervals (with typical genetic and diagenetic constituents). ZEISS Primotech optical microscope was used for petrographic analysis, which was done at Utrecht University. The thin sections are 30 µm in thickness, and the rock material was previously impregnated with blue epoxy in a vacuum to visualize most of the connected porosity, which would be in blue. The petrographical analysis included a point-counting method using JMicroVision (Roduit, 2019), which is a high-definition image analysis toolbox for calculating and measuring picture components. We used it to determine the percentages of grain, matrix, porosity, and cement. The petrographic analysis of thin sections allowed us to group the studied rock facies into microfacies based on sedimentological and diagenetic characteristics.

5.4 Micro CT

One sample from HRL_02 at 1061.1 m of the core was used for X-ray micro-Computed Tomography (Micro-CT) at IFP Energies Nouvelles (France). The use of high-resolution X-ray scanning, a non-destructive technique producing multiple 2D pictures, allowed us to determine density-associated heterogeneities in a representative sample at a 20µm scale. Consequently, 3D volumes consisting of 2D photos in several slices through the samples were created. Each image (or slice) is displayed as a grayscale colormap depicting the attenuation of how the X-ray travels through the sample of the rock. (Cappuccio, et al. 2020). Where the X-ray travels through empty space (e.g., fractures and pores), it is colored black in the generated image. As the grey level passes through solid material (well-cemented samples or sections), the generated image will incline toward white color. An insight into the fracture network is described and characterized by the 2D images and 3D models. The bioturbation, stylolites and fracture distributions are illustrated and analyzed.

6. Results

6.1 Sedimentological Core description

6.1.1 HRL_02 Core

The 22m long HRL_02 core (Figs. 9, 10) is composed of mostly white chalky limestone made up of very-fine calcium carbonate grains interbedded by millimeter-scale, bed parallel stylolite seams associated with sub-horizontal microfractures (Figs. 11a, 11b). The hardness gradually softens (upwards?) as observed by the highly fractured interval at the bottom of the core (Fig. 10). There are several low-angle clay-filled thin stylolites showing dark gray colors (11a, 11b) in the more heterogeneous interval of the core. In fewer intervals, the core is homogenous (Fig. 11c). Plug porosity measurements have been previously achieved, indicating that the bulk porosity ranges from 11% to 33%, and the permeability ranges from 0.1 mD to 10 mD (NLOG). The core will be described in terms of the intensity of stylolite seams meaning the number of seams encountered in a certain interval and the intensity of bioturbation.

HRL_02 core (Fig. 12) has a high stylolite seams intensity interval (Zone 1), and medium bioturbation is encountered at its uppermost part (from 1060.4 m to 1062.4 m), with grains fining from wackestone to mudstone towards the stylolites. A medium intensity of stylolite seams (Zone 2) is present in the interval from 1062.4 to 1073.9. The bioturbation intensity is medium from 1062.4 m to 1065.9 m, which increases to high intensity from 1065.9 m to 1071.4 m, and then decreases to medium intensity from 1071.4 m to 1078.4 m. The intensity of the stylolite seams in the core's last section (deepest part) is very high (Zone 3), ranging from 1073.9 m to 1082.4 m, with medium bioturbation intensity that tends to increase towards the bottom (Fig. 12).

Figure 9: HRL-02 Core depth from 1060.4 to 1064.4. This represents the top of the core which is mostly chalky limestone with interbedded clay and minor sub-horizontal.

Figure 10: HRL-02 depth ranges from 1078.4 m to 1081.9 m. This represents the base of the core which is highly fractured compared to the top of the core.

(A): Depth: 1062.15.
Chalky limestone with sub-horizontal fractures interbedded by clay.

(B): Depth: 1062.3.
Chalky limestone with low angle interbedded clay no fractures present.

(B): Depth: 1065.95.
Homogeneous chalky limestone no fractures and no clay interbedded.

Fig. 11: Zoomed-in pictures show the different characteristics and textures encountered in the HRL_02 core.. The description and depth is specified below each picture.

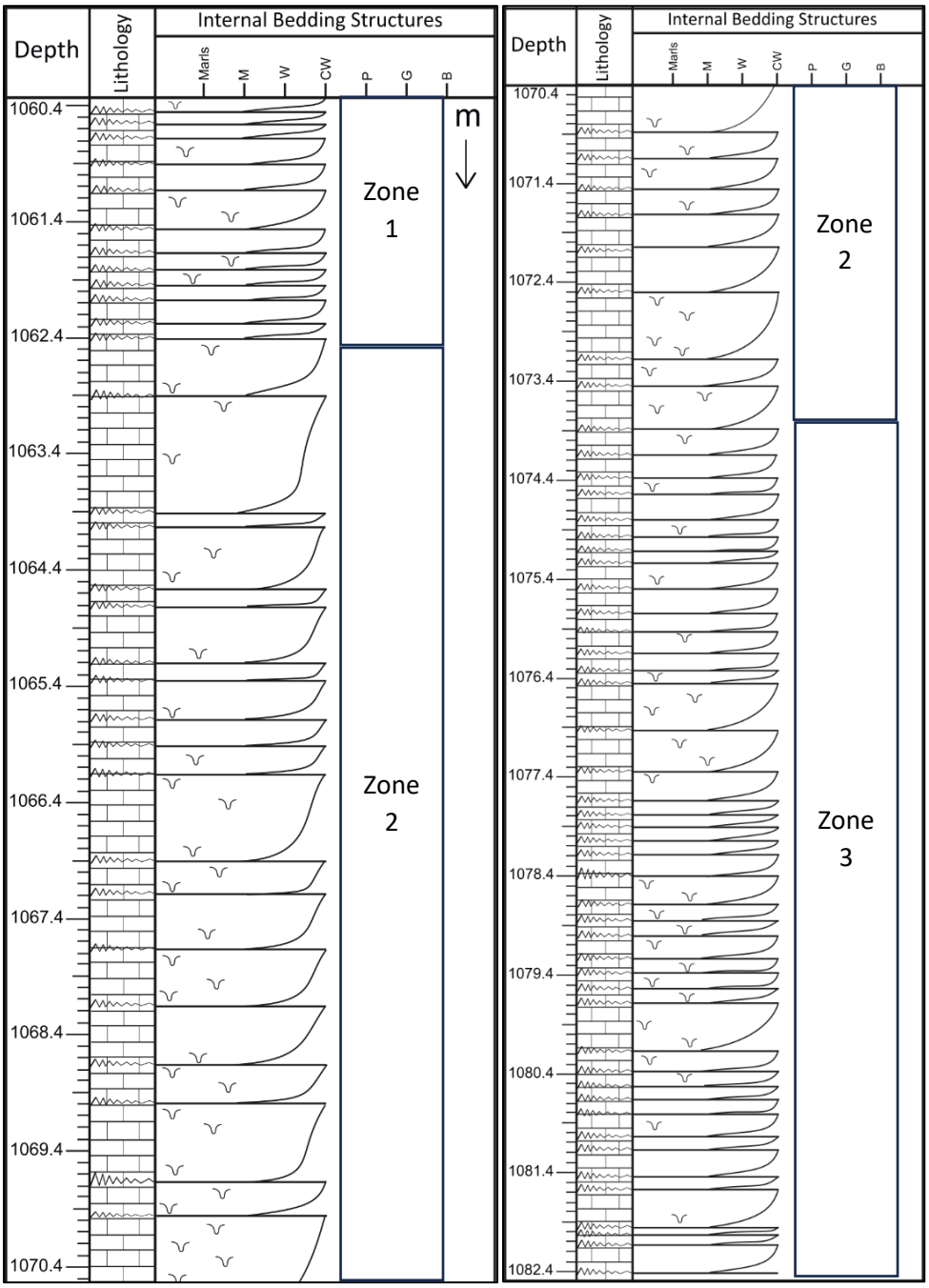

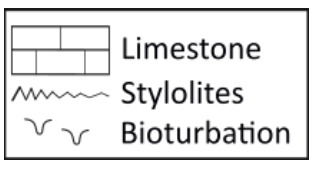

Figure 12: HRL_02 core description of the Ommelanden formation from 1060.4m to 1082.4m.

6.1.2 HRL_04 Core

The core is composed of 4 meters of dark gray shales and 7 meters of beige chalky soft limestone, which is micro-fractured throughout (Fig. 13). The boundary between the shale and chalk is made up of conglomerates with different colors of clasts. Petrophysical analyses that were previously done indicate porosity ranges from 35.5% to 22.6% and permeability ranges from 40.7 mD to 0.42 mD (NLOG). The core is described in terms of the intensity of stylolite seams, meaning the number of seams encountered in a certain interval and the intensity of bioturbation, like the approach followed when investigating the HRL_02 core.

Shale from 1034 m to 1037.8 m makes up the uppermost part of the HRL_04 core, with a conglomerate of 2 cm forming the transition between shale and chalky limestone (Fig. 14). The chalky limestone is the rock type for the rest of the core, from 1038 m to 1058 m, with variations in the intensity of stylolites and bioturbation. The stylolite seams' relative intensity is higher (Zone 1) from 1038 m to 1052.2 m and changes to medium intensity (Zone 2) towards the base of the core at 1058 m (Fig. 14). The bioturbation intensity is medium from 1038 m to 1054 m and changes to high until 1056 m, then changes to low towards the core's base at 1058 m.

Figure 13: The core represents two intervals. The shallower section, which is composed of mainly dark grey shales depth ranges from 1034 m to 1039 m. The deeper section is highly fractured beige chalky limestone depth ranges from 1052m to 1058m.

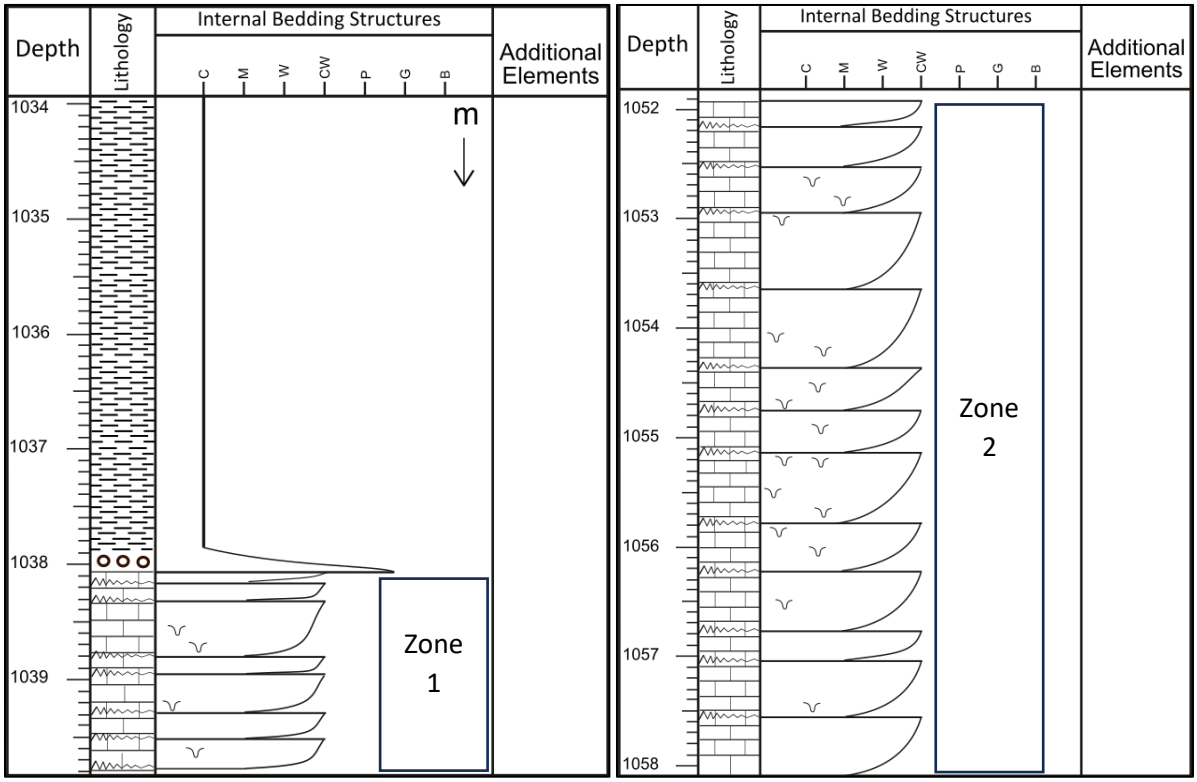

Fig 14. HRL_04 core description of the Ommelanden formation from 1034m to 1039.8.4m and from 1052m to 1058m.

6.2. Wireline logs and Petrophysical Analyses

6.2.1 HRL_02 logs

The Gamma Ray values of HRL_02 range between 18 API and 27 API, which fall in the typical Gamma Ray ranges for chalk formations. There are low-frequency cycles from low GR to high GR every 2 m in the uppermost part of the core from 1060 m to 1069 m which indicate alterations between clean chalk and higher clay or radioactive elements. In the other parts of the core, the cycles are higher in frequency, from low GR to high GR every 1 m, suggesting there is a higher intensity interval of clay or radioactive elements.

The Neutron log values could be a first approximation to relative porosity over the core. The values range between 680 gAPI and 820 gAPI, with higher interval values of more than 750 in the uppermost part of the core from 1060 m to 1077. In comparison, the lowermost part of the core has lower values (less than 750 gAPI), ranging from 1077 m to 1080 m. There are three porosity plug readings of 27% at 1065 m, 1070 m, and 1075 m. These readings correspond to the high neutron values in the upper part of the log. The porosity in the fourth plug is 19 % at 1080 m depth and corresponds to the lower porosity approximated by the lower neutron values in the bottom part of the core from 1078 m to 1083 m.

The induction log could be another good indicator of porosity since higher induction values correspond to higher relative porosity and lower induction values correspond to lower porosity values. The trend of the induction log generally follows the same trend as that of the neutron log, where higher induction values are in the upper part of the core and lower induction values are in the bottom 2.5 meters of the core.

The horizontal permeability is measured in the core, resulting in 0.8 mD at 1065 m, 1070 m, and 1075 m (Fig. 15). The permeability value is almost 1 mD at 1080 m, which is slightly higher than the three above-mentioned values. Yet they remain very low permeability values (expected permeability values in chalk reservoirs). Additional permeability readings were acquired throughout the core using TinyPerm 3. The values are not as accurate as plug permeability but are useful for comparing relative permeability throughout the core. The values range between 120 mD and 200 mD, with relatively higher values in the top 6 meters and the bottom 2 meters (Fig. 15).

The density values are between 2.18 kg/m3 and 2.32 kg/m3. T values vary every half a meter. The variations in the density values could be attributed to many factors, such as mineralogy, compaction, cementation, and dissolution. The low-density values are correlated with high porosity values at the porosity plug samples and air permeability measuring more than 150 mD at 1063, 1065.5, 1069.9 m, and 1080 m (Fig. 15).

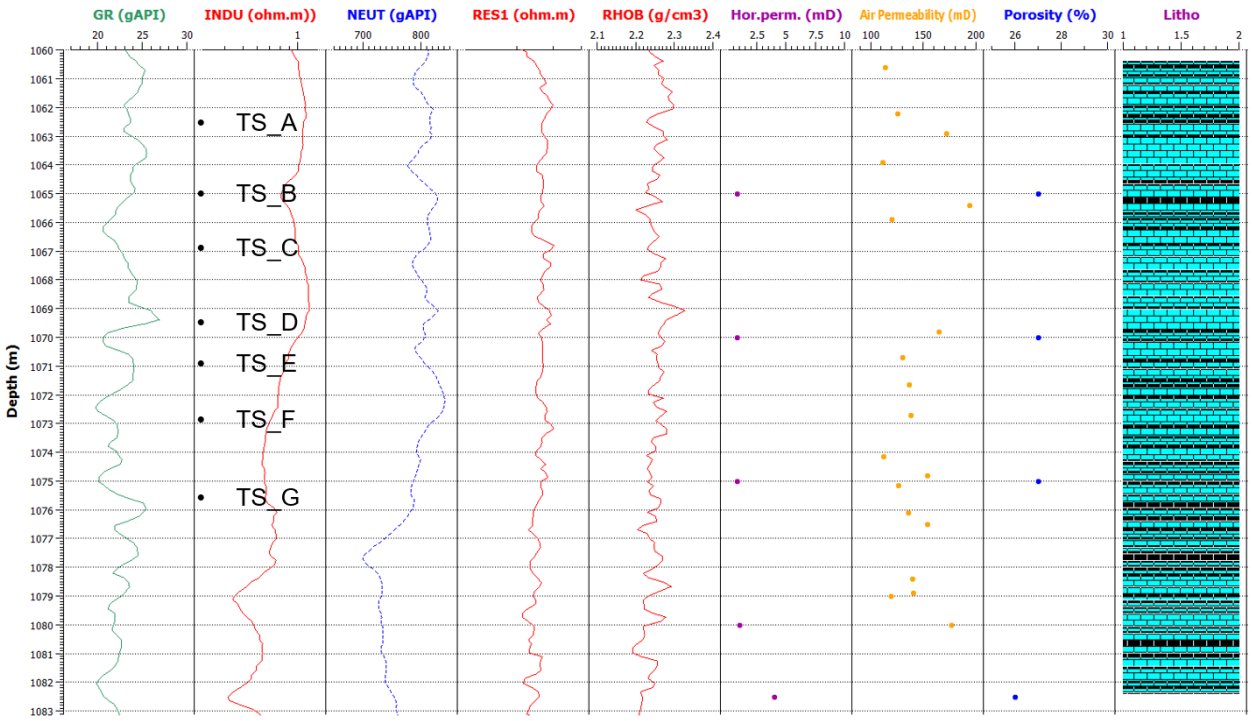

Figure 15: A panel showing the HRL_02 petrophysical logs correlation and analysis using EasyTrace software (TS_A to TS_G, showing the locations of the thin sections).

6.2.2 HRL_04 logs

The gamma-ray (GR) (Fig. 16) values range between 6 gAPI and 17 gAPI in the investigated core interval of HRL_04 well. The value increases from 8 gAPI at 1051.75 m to 14 gAPI at 1053 m, then drops to 7 gAPI at 1053.75 m. The value of GR increases from 7 gAPI to 14 gAPI at 1054.75 m, then gradually decreases to 6 gAPI at 1057 m, and at last increases steadily with depth until the end of the interval at 1058 m.

The RHOB log values indicate the formation's bulk density and range from 2.18 g/cm3 to 2.3 g/cm3 throughout the 1051 m to 1058 m interval. The overall trend of the formation density increases with depth, with small alterations at the shallower depth, particularly a spike of 2.25 g/cm3 at 1052.3 m and a drop to 2.18 g/cm3 at 1052.9 m. The value of the density log increases gradually to a peak of 2.29 g/cm3 at 1055.75 m, then decreases to 2.22 g/cm3 at 1056.5 m. At 1057 m, the density increases slightly by 0.2 g/cm3, then returns to 2.22 g/cm3 at 1057.5 m, and gradually increases with depth to a little over 2.3 g/cm3 at 1058 m.

The neutron porosity log values range between 22 PU and 26 PU. The overall trend fluctuates every 1.5 m between high and low values. The neutron log's lowest value is 22 PU at 1052.5 m, 1054.4 m, and 1055.5 m. The neutron log has three spikes to 26 PU at 1055 m, 1057 m, and 1057.75 m.

The DT log is the sonic log, and the values range from 100 µs to 125 µs. The cyclicity of the log is lower frequency that of other logs, there are only two cycles of low to high fluctuation. The lowest values are at 1052.5 m, 1054.5 m, 1055.75 m, and 1058 m. The values of the DT log at these lowest depths are 115 µs, 110 µs, 105 µs, and 100 µs, respectively. The sonic log spikes to 125 µs at 1053.75 m and 1056.75 m.

Grain density, vertical permeability, horizontal permeability, and porosity were determined by plug samples taken from the core. Throughout the interval, the grain density is relatively constant in all plug samples, ranging from 2.67 to 2.69 g/cm3. The permeability plug sample measurements range between 0.33 mD and 8.5 mD. The majority of core permeability measurements are between 1 mD and 3 mD. The higher permeability values were from 7 mD to 8.5 mD at 1052.4 m, 1055.4 m, 1056.1 m, and 1056.4 m. The plug porosity measurements of the interval range from 22.7% to 33%. At depths of 1053.1 m, 1055 m, and 1057.8 m, porosity is lower than 25%. The remaining porosity values are all above 25%, with the highest above 30% at the following depths: 1052.5 m, 1053.5 m, 1053.9 m, 1054.6 m, 1055.4 m, 1055.7 m, 1056.1 m, and 1056.7 m.

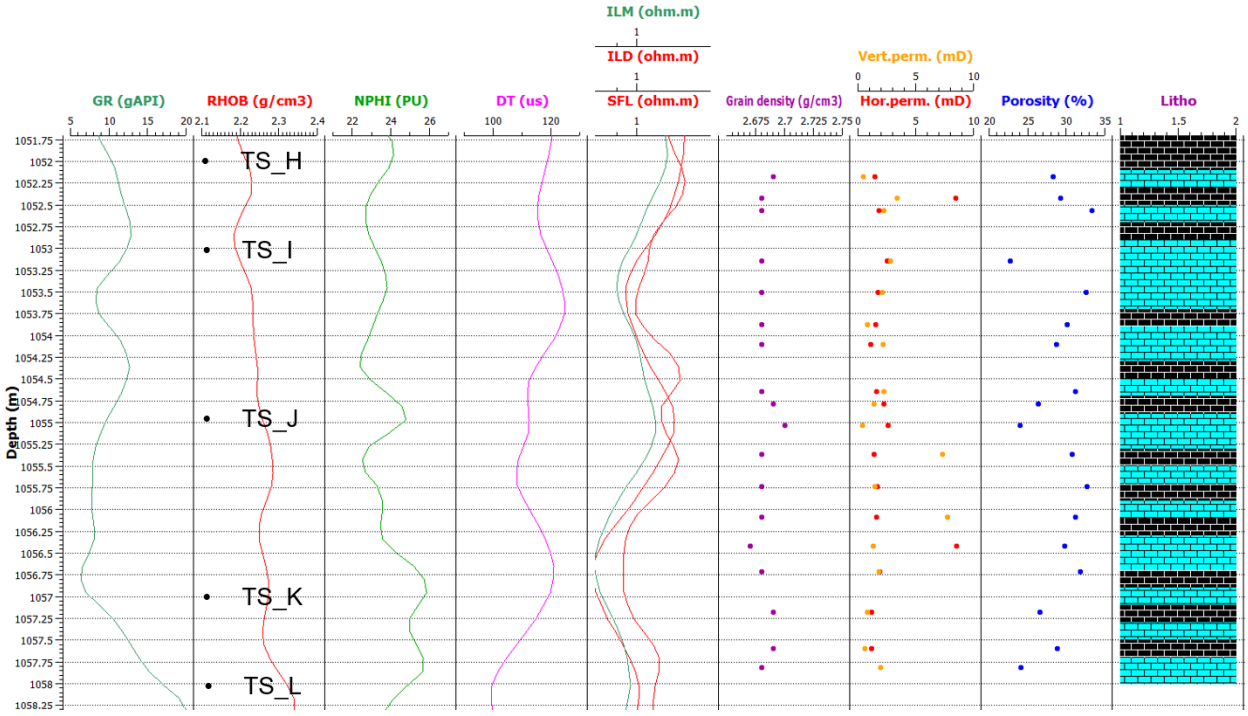

Figure 16: HRL_04 master petrophysical logs for correlation and analysis using EasyTrace.

6.3. Petrographic Analysis

6.3.1 HRL_02 Well Core

Thin Section A

Thin section A (Fig. 17) is at a depth of 1062.65 m. It represents a sponge-dominated wackestone. The total grains amount to 22%, and the matrix is 76%. More than half of the grains are 250 to 350 µm in size, mostly sponges. The remaining grains are less than 50 µm in size, which are foraminifera, coccoliths, and micrized grains. The thin section shows prevailing microporosity and cement-reduced secondary moldic porosity of 2%.

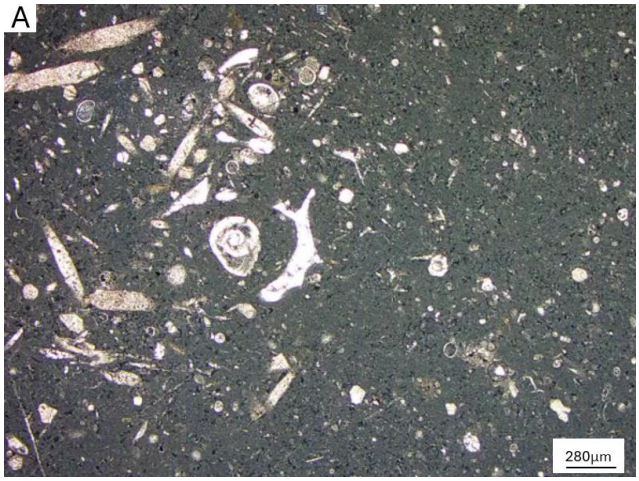

Figure 17: Plane-polarized light view (PPL) micrograph of TS_A showing a wackestone to packstone at 1062.65m depth (HRL_02 well core).

Thin Section B

The thin section B (Fig. 18) at a depth of 1065.2 meters, shows a foraminifera-dominated wackestone to mudstone. The total grains are 15%, and the matrix is 83%. More than half of the grains range in size between 150 µm and 250 µm, and the remaining are less than 50 µm. It is moderately bioturbated, as can be observed by localized zones with disturbed matrix and grains with clear cutting/perforation fronts, showing changes in the general matrix colors tending towards a brownish tinge (Fig. 18). The burrowing infill consists of finer mud with a few grains (Fig. 19). The thin section shows a microporous texture and cement-reduced secondary moldic porosity of 2%.

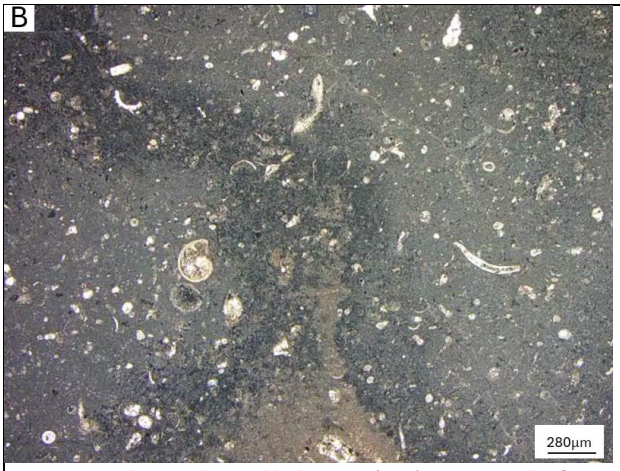

Figure 18: Plane-polarized light view (PPL) micrograph of TS_B from HRL_02 showing a wackestone to mudstone at 1065.2m depth (HRL_02 well core).

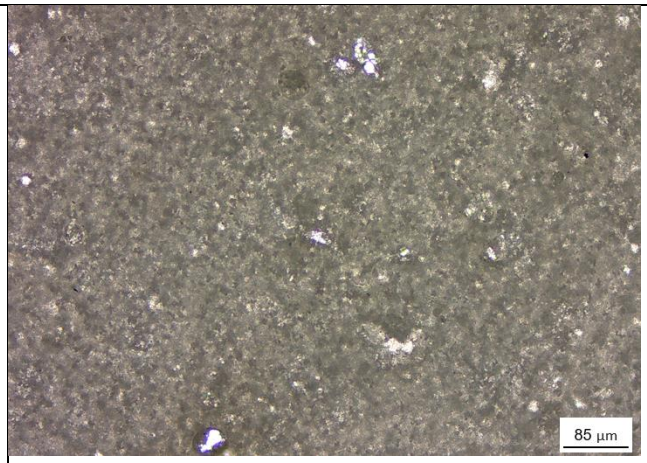

Figure 19: Zoomed in Plane-polarized light view (PPL) micrograph of TS_B from HRL_02 at 1065.2 m depth showing finer matrix than rock texture and fine silt size scattered fossils fragments.

Thin Section C

The thin section C (Fig. 20), located at a depth of 1066.9 meters, displays a wackestone-to-mudstone texture. The total grains are 14%, of which 9% have average grain sizes less than 50 µm and 5% range from 150 µm to 250 µm. The matrix covers the remaining 85%. It is moderately bioturbated and fractured. It has microporosity, cement-reduced secondary moldic porosity of 1%, and open

fractures. The bioturbation zone (Fig. 21) has more clay than the rest of the thin sections. We observe small stylolites and sutured seams lining the clay flasers, indicating a probable recrystallization that has slightly increased the matrix grain sizes locally (Fig. 21).

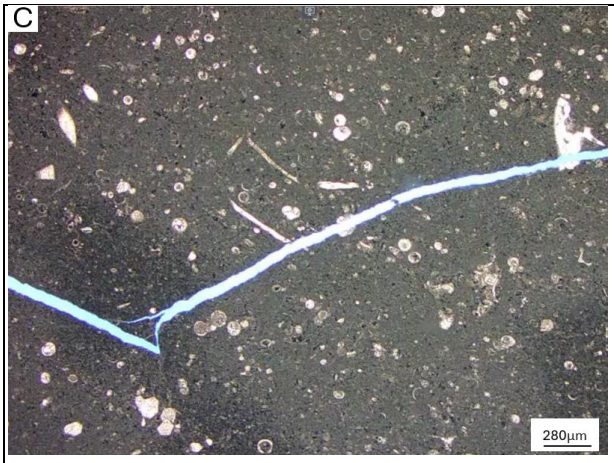

Figure 20: Plane-polarized light view (PPL) micrograph of TS_C from HRL_02 showing wackestone to mudstone at 1066.9m depth (HRL_02 well core). Open fractures are also observed in this thin section.

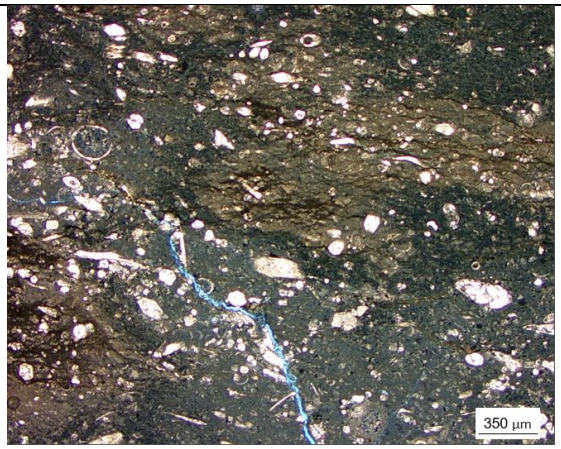

Figure 21: Plane-polarized light view (PPL) micrograph of TS_C showing medium sand size grains and clay flasers more grainy than the rock texture at 1066.9 m depth (HRL_02 well core). Open fractures are also observed in this thin section.

Thin Section D

The thin section D (Fig. 22), at a depth of 1069.6 meters, displays wackestone to mudstone. The total grains are 22%, of which 11% are less than 50 µm in size, and 11% have grain sizes from 150 µm to 250 µm, The matrix is 77%. The material exhibits moderate bioturbation and fractures along its bioturbation path, as shown in Figure 23. It has a cement-reduced secondary moldic porosity of 1%. This thin section also shows common open fractures. The bioturbated zones appear to be where stylolite seams are frequent, grain sizes are slightly coarser (probably by recrystallization or due to original sediment deposition during bioturbation), and later fractures occur (see Fig. 23).

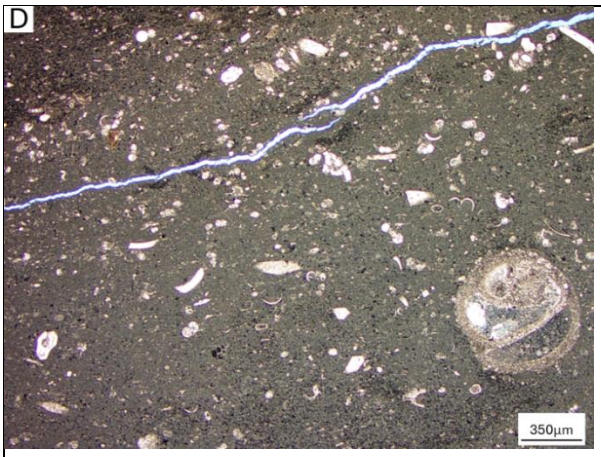

Figure 22: Plane-polarized light view (PPL) micrograph of TS_D from HRL_02 showing wackestone to mudstone at 1069.6m depth (HRL_02 well core). Open fractures are also observed in this thin section.

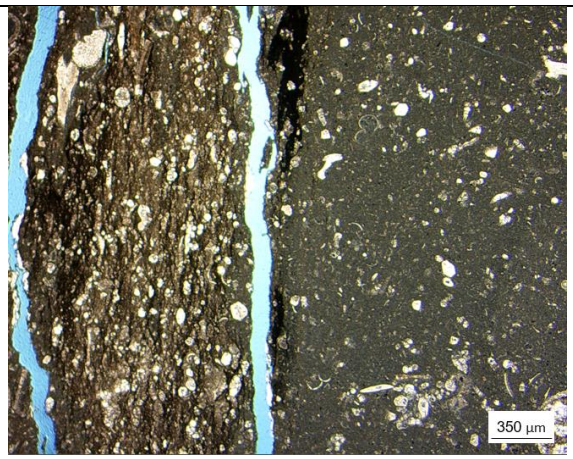

Figure 23: Plane-polarized light view (PPL) micrograph of TS_D showing the bioturbation texture has whitish cemented matrix and a higher percentage of grains than the rest of the rock at 1069.6 m depth (HRL_02 well core). Open fractures are also observed in this thin section.

Thin Section E

The thin section E (Fig. 24) at a depth of 1071 meters is a wackestone to mudstone containing 18% grains and 81% matrix. 9% of the grains are less than 50 µm in size, and the other 9% have sizes ranging between 150 µm and 250 µm. It is moderately bioturbated, with silicification preferentially occurring in the burrowed zones (Fig. 25). There is no evidence of fractures. It has a cement-reduced secondary moldic porosity of 1%.

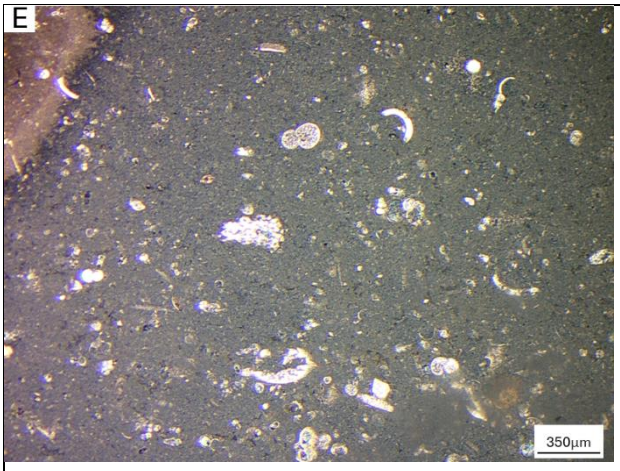

Figure 24: Plane-polarized light view (PPL) micrograph of TS_E from HRL_02 showing wackestone to mudstone at 1071.1m depth (HRL_02 well core).

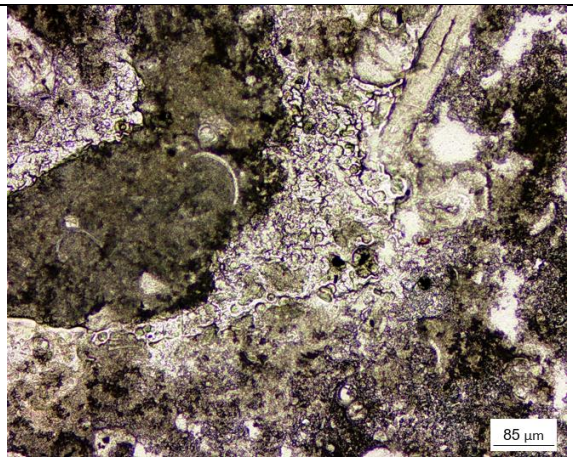

Figure 25: Plane-polarized light view (PPL) micrograph of TS_E from HRL_02 at 1071.1m depth showing silicification in bioturbated zone (HRL_02 well core).

Thin Section F

The thin section F (Fig. 26) at a depth of 1072.8 meters is a wackestone to mudstone, with 15% grains and 79% matrix. 9% of the grains are less than 50 µm in size, and 6% have grain sizes between 150 µm and 250 µm. It is moderately bioturbated, with a finer matrix and fewer grains in the bioturbated

zone (Fig. 27). This thin section shows fractures with undulating sides, typical of dissolution (Fig. 26). It has microporosity and cement-reduced secondary moldic porosity of 6%.

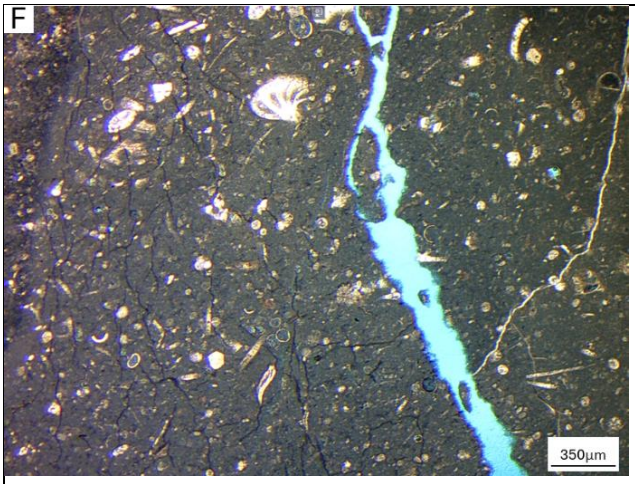

Figure 26: Plane-polarized light view (PPL) micrograph of TS_F from HRL_02 showing wackestone to mudstone at 1072.8m depth (HRL_02 well core). Open fractures are also observed in this thin section.

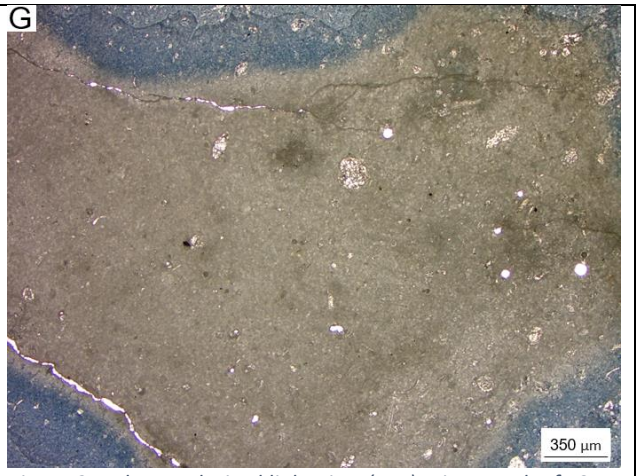

Figure 27: Plane-polarized light view (PPL) micrograph of TS_F showing 1-3% grains and finer matrix in the bioturbation at 1072.8 m depth (HRL_02 well core).

Thin Section G

The thin section G (Fig. 28), at a depth of 1075.6 meters, is a wackestone-to-mudstone with 13% grain and 87% matrix. More than half of the grains are less than 50 µm in size, and the rest are between 150 µm and 250 µm, except for two exceptionally larger grains of 400 µm in size. It is highly bioturbated, as can be seen by the brownish color and the clay presence in the black color. There is no visual porosity, but the thin section displays a microporous texture.

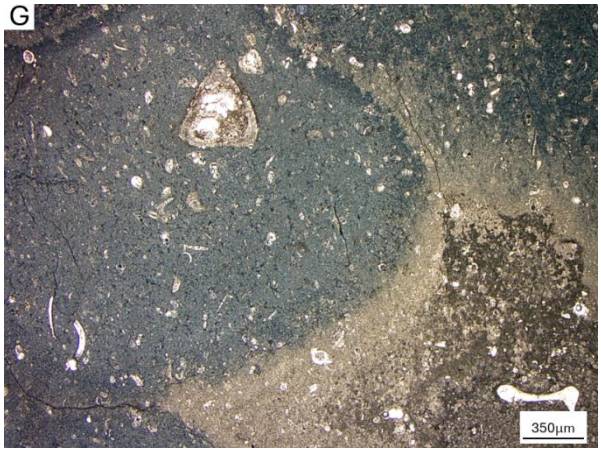

Figure 28: Plane-polarized light view (PPL) micrograph of TS_G from HRL_02 showing wackestone to mudstone at 1075.6m depth (HRL_02 well core).

6.3.2 Micro CT

We acquired one sample for a micro CT analysis at 1061.1 m depth from the HRL_02 well core to identify the microfractures and assess the permeability. Sponge spicules display a white color and needle-like shape, as do other biogenic grains. The Micro-CT 2D sections and 3D images (Fig. 29) clearly outline the open stylolites. The two figures clearly show intense bioturbation and identify 7 sub-horizontal microfractures from top to bottom. These open stylolites have an inclined lateral (horizontal) extension with discontinuous pore space in their 3D pattern. The fracturing of the various compaction stylolites that are associated with the bioturbation architecture shows a complex and discontinuous pore space. While some fractures are more continuous than others in the horizontal direction, they do

not appear to connect vertically and remain isolated. The intensity of these fractures would allow the flow of injected CO2 or any fluids into the host-rocks. More research on modeling the fracture network and understanding it could be beneficial to ensure the flow regimes and tortuosity in such complex conduits.

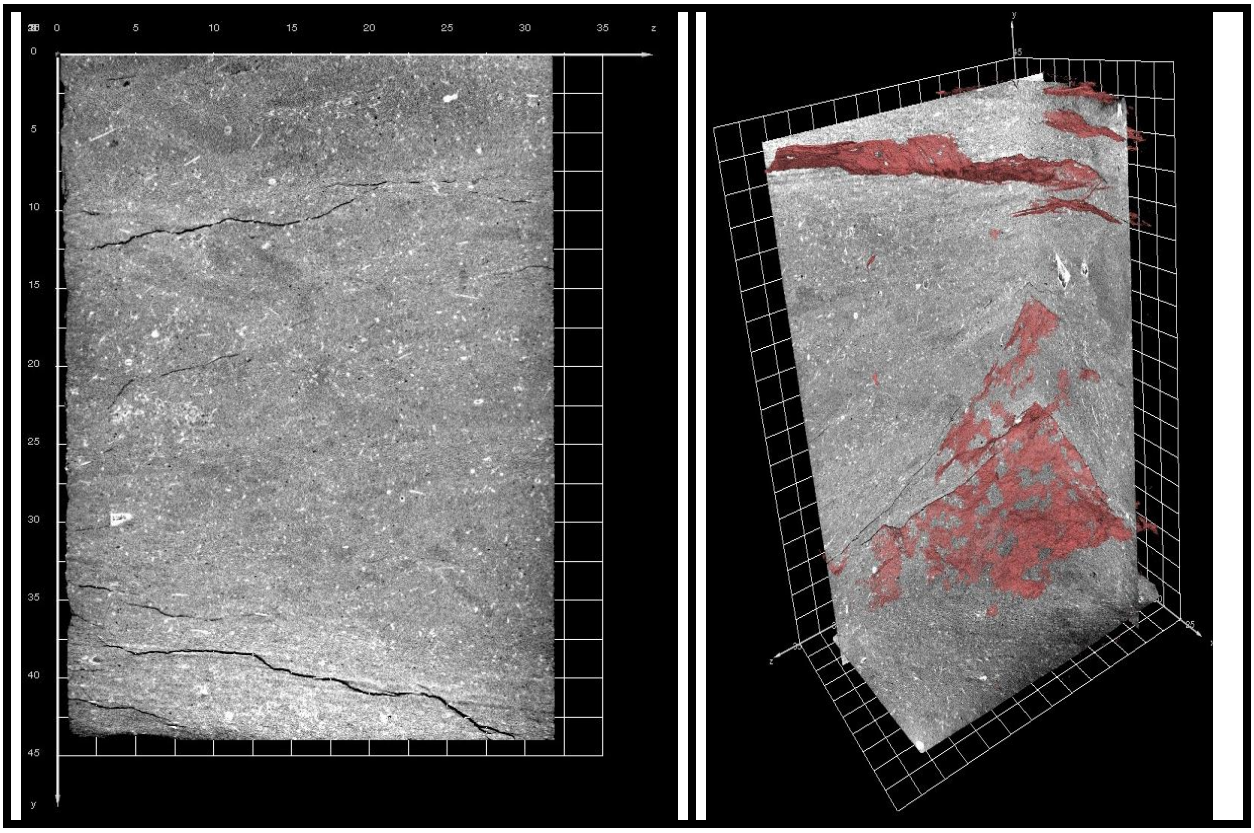

Figure 29: Micro CT scan of HRL_02 sample at 1061.1m. The scan scales (horizontal and vertical) are in mm and the resolution is at 20µm.

6.3.3 HRL_04

Thin Section H

At a depth of 1052 m, Thin Section H (Fig. 30) exhibits a wackestone composition of 30% grains and 64% matrix. 16% of the grains are less than 50 µm in size, and 14% have grain sizes between 150 µm and 250 µm. The thin section shows moderate bioturbation and very thin open fractures with undulating sides typical of dissolution (Fig. 30). The burrowing infill consists of finer mud with fewer dissolved grains (Fig. 31). It displays a microporous texture and has 6% cement-reduced secondary moldic porosity.

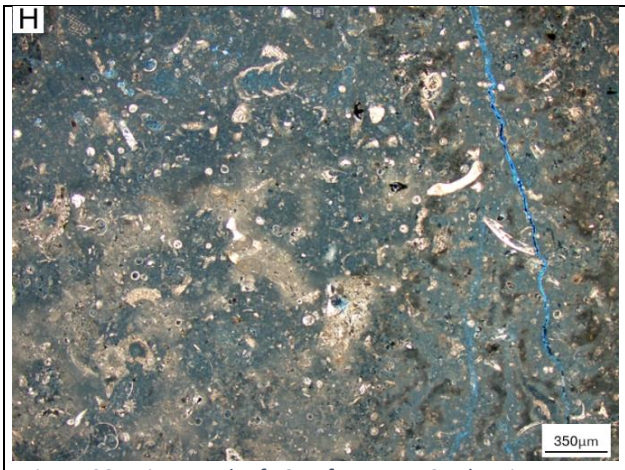

Figure 30: Micrograph of TS_H from HRL_04 showing wackestone at 1052m depth (HRL_04 well core). Open fractures are also observed in this thin section.

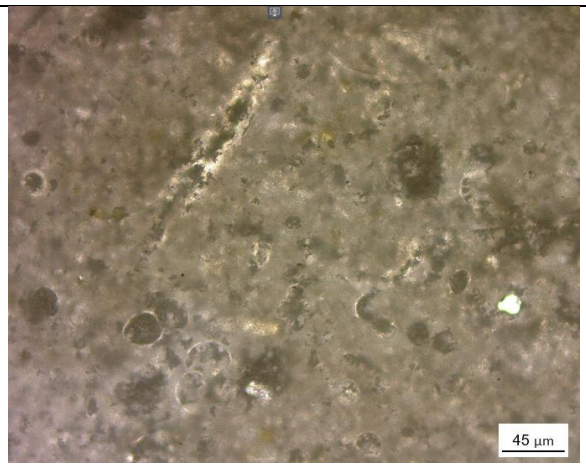

Figure 31: Micrograph of TS_H from HRL_04 showing finer matrix and scarcity of grains at 1052 m depth (HRL_02 well core).

Thin Section I

Thin section I (Fig. 32) is at a depth of 1053.5 m and is a wackestone to mudstone with 21% grains and 74% matrix. 14% of the grains are less than 50 µm in size, and 7% range from 150 µm to 250 µm. It is highly bioturbated and highly fractured. Silicification appears to be selective for the bioturbated areas (Fig. 33). It has microporosity and 5% cement-reduced secondary moldic porosity. Open fractures are thin and irregular (typical of dissolution).

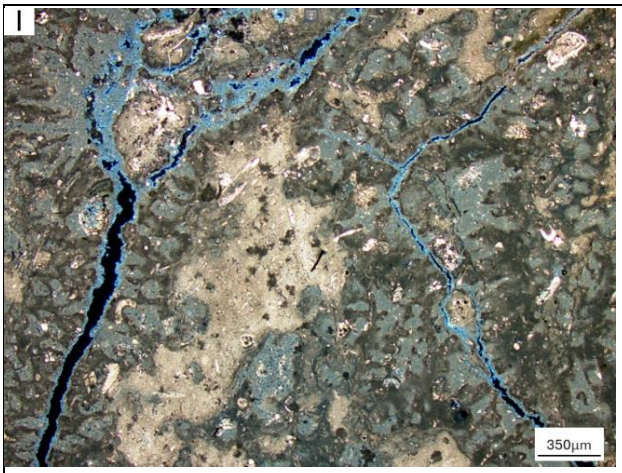

Figure 32: Micrograph of TS_I from HRL_04 showing wackestone to mudstone at 1053.5 m depth (HRL_04 well core). Open fractures are also observed in this thin section.

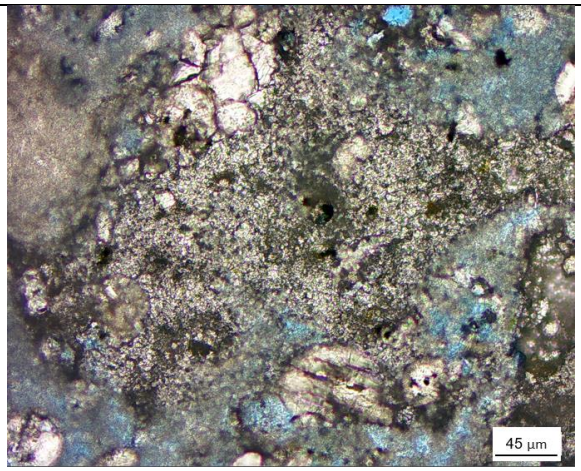

Figure 33: Micrograph of TS_I showing silicification in bioturbation at 1053.5 m depth (HRL_04 well core).

Thin Section J

Thin section J (Fig. 34), at a depth of 1055 meters, is a sponge-dominated wackestone with 32% grains and 60% matrix. 17% of the grains are 50 µm in size, and 13% are from 150 µm to 250 µm in size.

It is highly bioturbated and contains thin fractures. It has a cement-reduced secondary porosity of 5%. There are small traces of phosphatization (3%) in bioturbated areas (Fig. 35).

Figure 34: Plane-polarized light view (PPL) micrograph of TS_J from HRL_04 showing wackestone at 1055 m depth (HRL_04 well core). Open fractures are also observed in this thin section.

Figure 35: Plane-polarized light view (PPL) micrograph of TS_J from HRL_04 showing phosphatization in bioturbation.

Thin Section K

The thin section K (Fig. 36), located at a depth of 1057 meters, is classified as a wackestone to mudstone, containing 20% grains and 77% matrix. 10% of grains are less than 50 µm in size, and 7% are between 150 µm and 250 µm. It is highly bioturbated and fractured. The matrix texture indicates microporosity and has a cement-reduced secondary moldic porosity of 3%. Open fractures are relatively thin, with irregular and undulating patterns typical of dissolution.

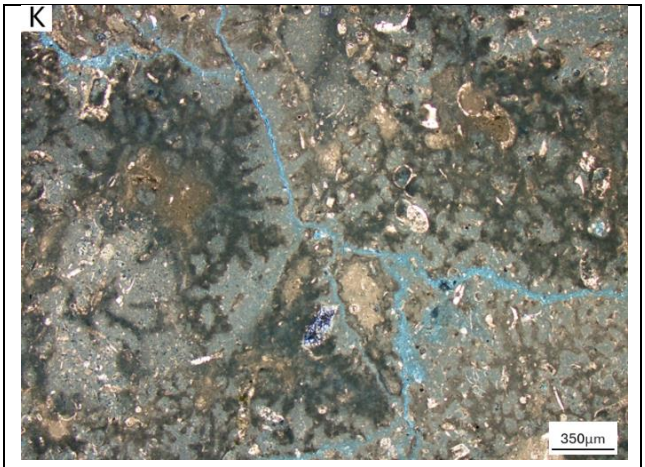

Figure 36: Plane-polarized light view (PPL) micrograph of TS_K from HRL_04 showing wackestone to mudstone at 1057 m depth (HRL_04 well core). Open fractures are also observed in this thin section.

Thin Section L

The thin section L (Fig. 37) at a depth of 1058 meters is a sponge-dominated wackestone to packstone that has 19% grains and 79% matrix. 7% of the grains are 50 µm in size, and 12% are from 150 µm to 250 µm. It is highly bioturbated, with thick, open fractures. There are rare, small traces of glauconite (Fig. 38). It has a cement-reduced secondary moldic porosity of 2%. The margins of the bioturbated zones also display stylolitic or sutured patterns and are often opened into fractures.

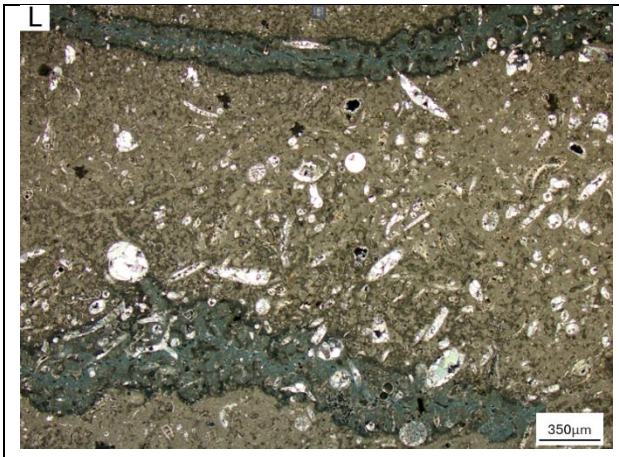

Figure 37: Plane-polarized light view (PPL) micrograph of TS_L from HRL_04 showing wackestone to packstone at 1058 m depth (HRL_04 well core). Stylolitic and open fractures are also observed in this thin section.

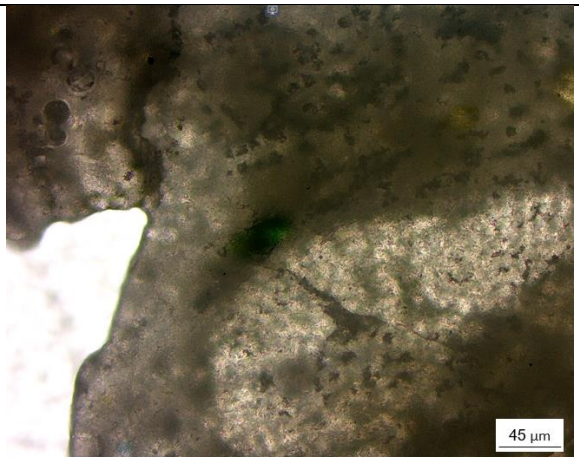

Figure 38: Plane-polarized light view (PPL) micrograph of TS_L from HRL_04 showing glauconite in bioturbation at 1058m depth (HRL_04 well core).

7. Discussion

7.1 Chalk Bioturbated Facies

Most of the investigated well cores in the two wells (HRL_02 and HRL_04) show uniform pervasive bioturbation, stylolitization, and horizontal fractures with varying intensity that is demonstrated by the clayey interlayers (pointing to a possible depositional cyclicity). The entirely bioturbated fabric and the absence of primary sedimentary structures point to oxygenated benthic environments with a relatively shallow marine depositional environment, as has been previously documented by van der Molen (van der Molen, 2004). These circumstances allowed the infauna to burrow the sediments on the sea floor, removing the original sedimentary texture. The variety of trace fossils and the scarcity of benthic fossils indicate a reasonably abundant infauna and a limited shelly epifauna, which suggests a significant nutrient input to the sea floor and their preservation (McKinney & Hageman, 2006). Because the sedimentary structures have been destroyed by bioturbation, it is impossible to ascertain the original depositional process. However, the slow accretion and very fine sediment grain size suggest that the pelagic process was primarily responsible for deposition, with relatively thin event layers potentially contributing as well. The lack of mineralization on intrapelagic erosional surfaces suggests that pelagic deposition is affected by bottom currents and sediment gravity over short periods of time rather than long periods of time, which are some of the most important factors that affect chalk deposition (Esmerode & Surlyk, 2009). The reworked sediments may have been transported away from the site instead of being resuspended locally and creating a post-event suspension deposit, as indicated by the absence of distinctive event deposits. Although the extent of erosion is hard to assess, the preservation of the surfaces suggests that erosion destroyed the softer topmost portion of the sediment column, where the most effective burrowing organisms would have predominated.

7.2 Bioturbation Effects

The core description of both HRL_02 and HRL_04 of the Ommelanden Formation indicates the association of bioturbation presence with higher stylolite intensity, contributing to reservoir quality enhancement through fractures. In the HRL_02 core (Fig. 12), Zone 1 (1060.4 m to 1062.4 m) and Zone 3 (1073.9 m to 1082.4 m) display high stylolite intensity and moderate to high bioturbation. Similarly, in the HRL_04 core (Fig. 14), Zone 2 (1038 m to 1052.2 m) shows high stylolite intensity and considerable bioturbation.

We looked at Thin Section I (Fig. 32) from the HRL_04 well core at a depth of 1053.5 m and observed that the cement reduced secondary moldic porosity to one of the highest levels, at 5%. However, bioturbation selective silicification reduced bulk rock porosity to the lowest measured plug porosity of 22.7%, compared to other core samples where measured plug porosity was more than 30%. Thin Section I was also one of the highly fractured thin sections (Fig. 32). Another highly fractured thin section was Thin Section J from HRL_04 at 1055 m depth, which was also highly bioturbated and considered to have a high moldic porosity of 4%. Still, its bulk porosity was one of the lowest, based on the plug porosity measurement of 24%. In HRL_02 thin section A at 1062.65 m, the thin section displays no bioturbation and no fractures. In moderately bioturbated thin sections such as thin sections (C, D, and F) at depths of 1066.9 m, 1069.9 m, and 1072.8 m, respectively, some fractures were observed (Fig. 20, 22, and 26) but were less predominant than in more bioturbated thin sections. Both the core description and thin sections of data support the observation that high bioturbation in the Ommelanden Formation is strongly associated with stylolites and fracture development.

From these results, one can conclude that bioturbation plays a vital role in the control of the porosity and permeability of the reservoir rocks. Bioturbation influences sedimentation through feeding, hence ingestion, transportation, and segregation (Bromley 1996). This process creates heterogeneities that influence reservoir quality, as highlighted in this paper from the thin-section petrography and the well sedimentary logs.

These findings confirm previous studies, which have illustrated some of the positive and negative implications of bioturbation on reservoirs. Bioturbation can improve porosity and permeability through the development of natural fractures and connected reservoir networks from burrow structures (Knaust et al., 2020). The bioturbation's effects may vary greatly based on geometry, orientation, degree, infill, and diagenesis (Tonkin et al., 2010; Salih et al., 2021). It could negatively impact the reservoir by reducing the porosity and permeability, according to the work of Qi et al. (2012) and Abdlmutalib et al., (2022).

There are a couple of points highlighted in these observations that point toward the multifaceted influence of bioturbation in determining the petrophysical characteristics of sedimentary reservoirs while opening up the case for the need for a more nuanced view of the impacts of bioturbation in the evaluation of reservoir quality (Baniak et al., 2022; La Croix et al., 2012; Friesen et al., 2017). With the exception of very few papers, no one has done an overall analysis of the impact of bioturbation on the reservoir properties of the Ommelanden Formation in relation to its suitability for CO2 storage.

7.3 Chalk Diagenetic Events

1. **Deposition in an Oxygenated Environment:**

   The accumulation of calcium carbonate organisms such as foraminifera, sponges, and coccoliths is an indication of the shallow marine, well-oxygenated environment of the Ommelanden Formation. The analysis of HRL_02 and HRL_04 thin sections provides an insight into grain-to-matrix ratios across different depths of the two cores.

   In HRL_02 core, the grain-to-matrix ratios of different thin sections vary slightly in different samples and indicate a matrix-dominated composition. At 1062.65 m of HRL_02, Thin Section A (Fig. 17), the sponge-dominated wackestone grain-to-matrix ratio is 22% to 76%. At a deeper depth (1065.2 m) of HRL_02, Thin Section B (Fig. 18), the foraminifera-dominated mudstone has a lower ratio of 15% grains to 83% matrix. Another more predominant matrix is at 1069.6 m depth of HRL_02 in Thin Section D (Fig. 18), with a similar ratio of 22% grains to 77% matrix.

   There is more viability in the grain-to-matrix ratios of the HRL_04 core, indicating slightly different depositional and diagenetic conditions. At 1052 m depth of HRL_04, Thin Section H (Fig. 30), the sponge-dominated wackestone has a high grain-to-matrix ratio of 30% to 64%. A higher grain content is observed in Thin Section J (Fig. 34) at 1055 m of HRL_04; the grain-to-matrix ratio is 32% to 60%, suggesting higher energy in the depositional environment. On the contrary, less energy has affected the formation at the 1058 m depth of HRL_04, as evidenced by the lower grain-to-matrix ratio of 19% to 79% in Thin Section L (Fig. 37).

Variations in grain-to-matrix ratios of HRL_02 and HRL_04 indicate local differences in depositional energy and diagenesis. Grain content is typically higher in HRL_04 than in HRL_02, indicating that HRL_04 was more likely deposited under more dynamic conditions, i. Warszawa, 1971, and that there was more biogenic activity and more frequent sedimentation events.

These findings are corroborated by micrographs taken of the thin sections (Fig. 17–38) from both HRL_02 and HRL_02, which clearly show the majority of the marine fossils are well preserved. These fossils are mostly complete, and few are partially broken and have preserved their original shapes and types, suggesting an environment of consistent deposition. The differences in the grain-to-matrix ratio between the wells reflect the sedimentary heterogeneity and the possibility of increased porosity and permeability in the formation, which are favorable conditions for CO2 storage.

2. **Bioturbation and Finer Material Fill:**

In all thin sections examined, there are tube-like irregular burrowing structures that disturb the matrix and grains within the rock. Generally, the filling of these burrowing structures is finer, and some thin sections exhibit cementation. The grains filling the burrowing are fewer than the ones present in the (undisturbed) original fabric of the rock. There is no specific direction of burrowing, neither vertical nor horizontal. It has a rather random directionality. The bioturbation in the HRL_02 core is medium throughout the entire core interval, except for a higher intensity from 1065.4 m to 1073.9 m. The bioturbation intensity is medium in HRL_04 zone 1 (1038 m to 1058 m depth) and increases to higher in zone 2 (1056 m to 1058 m depth). Several thin section analyses show moderate bioturbation in HRL_02, such as Thin Section B, C, D, E, and F at 1065.2 m, 1066.9 m, 1069.6 m, 1071 m, and 1072.8 m, respectively. The bioturbations observed in the thin sections vary by the number of grains and the amount of cement filling these burrows. In most of the thin sections, the bioturbation is filled with a finer matrix of mud size and 1-5% grains, such as in (Figs. 19, 27, and 31). In HRL_02, in two thin sections C and D at 1066.9 m and 1068.6 m, the burrowings are filled with 20–30% grains (Fig. 21, 23, and 33), which indicates higher intra-fossil porosity compared to the thin sections with lower percentages of grains. Silicification is observed in HRL_02, Thin Section E at 1071 m (Fig. 25), and in HRL_04 at 11053.5 m (Fig. 33), which reduced the porosity. There is a very small percentage of phosphatized fossils in Thin Section J of HRL_04 at 1055 m (Fig. 35), and traces of glauconite are observed in Thin Section L of HRL_04 at 1058 m (Fig. 38).

3. **Dissolution and Cementation:**

All thin sections of the three microfacies exhibit the same digenetic characteristics, but the magnitude of diagenesis differs slightly. Observed general characteristics include partial grain dissolution, with several grains fully dissolved and filled with granular mosaic pore-filling cement. The cementation in pores is estimated to range from 5% to 15%, and calcite cementation is observed in the matrix. In the HRL_04 well core, the thin, irregular, and undulating fractures are typical of dissolution.

4. **Compaction and Stylolites Formation:**

Stylolite development is apparent from the core examination and thin section analysis of the Ommelanden Formation. These stylolites are mainly sub-horizontal in formation, and they play an important role in linking up the matrix microporosity and flow paths. They are well-defined and considered to be a positive contribution to the chalk system due to their transport capacity for fluids connecting the reservoir pore space, The below paragraphs will discuss the highest zones observed in HRL_02 and HRL_04 and their implications.

The HRL_02 core examination (Fig. 12) identified two zones of the formation with high stylolite intensity. These zones are located in two intervals of the core, from 1060.4 m to 1062.4 m and from 1073 m to 1082.4 m. In the HRL_04 core examination, only one interval, from 1038 m to 1058 m, showed a high intensity of stylolite seams.

Stylolite seams are 50–200 µm thick in the HRL_02 core and commonly develop in intervals that have intensified bioturbation. Stylolite seams were observed at 1066.9 m and 1069.6.6 m in Thin Sections C and D, which show moderate to high bioturbation (Figs. 20 and 22). Stylolites in these sections are oriented across the bioturbated layers, suggesting compaction and dissolution. The gamma-ray log of HRL_02 increased its value in the depth interval of 1071 m to 1078 m, which may indicate a higher clay content and could be interpreted as stylolite expression.

Stylolites in the HRL_04 core are thicker, 100µm–250µm, and are densely packed in the thin sections that have moderate bioturbation intensity, as in Thin Section J at 1055 m and Thin Section L at 1058 m, (Figs. 34 and 37). The HRL_04 Gamma-ray log readings are relatively higher between 1052 m and 1056 m, which is indicative of high clay content, and possibly correlated with the stylolite intensity.

In summary, stylolite intensity within the Ommelanden Formation are observed throughout both cores and thin sections, which are closely observed with bioturbation and could be indicated by high gamma rays. Their presence optimizes the existing connectivity and permeability in the formation, which is of great importance when sequestering CO2. The analysis of the thin sections and well logs allows synthesizing the information explaining the influence of stylolites on the formation of the reservoir parameters.

5. **Inversion, Uplift, and Fracturing:**

Two significant tectonic inversion episodes have greatly influenced the geological structural evolution of the Harlingen Gas Field, which played a major role in the reservoir characteristics. The first inversion took place in the Late Cretaceous and was strongly associated with the final stage of Chalk deposition. This period was critical because it led to uplift and subaerial exposure, which played a significant role in the development of veins observed in multiple HRL_02 and HRL_04 thin sections (Fig. 26, 30, 32, and 36). These open veins were primarily observed in HRL_04 thin sections, which have irregular and undulating patterns, indicating that their formation was likely driven by the infiltration of meteoric water and the dissolution of calcite during the uplift and exposure rather than stress changes from the inversion. This process is in agreement with the findings that have been indicated in other studies showing that chalk sedimentation and diagenesis are keenly influenced by the processes of erosion and subaerial exposure (Hancock, 1975; Ziegler, 1990). The diagnesis of chalk by calcite dissolution is a common process, often affected by acidic conditions from meteoric water infiltration (Zuddas & Mucci, 1994).

The second intense inversion episode was in the Oligocene and Middle Miocene, which caused an uplift and shift in the stress regime. This period was critical in the development of bed-parallel stylolites (BPS), which are commonly found at HRL_02 and HRL_04. Micro-CT scans show that these stylolites when opened, have discontinuous pore throats, and as such, the microstructure of the reservoir's permeability is intricate. This was most probably caused by heterogeneous stress distribution during inversion, where, while some stylolites are opened selectively, more or less compartmentalization is maintained. The presence of stylolites as is essential for improving lateral fluid transport and increasing reservoir permeability, according to Koehn et al. , (2012), Peacock et al. , (2017).

Overall, these inversion episodes have contributed to the evolution of a sophisticated fracture pattern, primary dissolution veins as part of the early diagenetic setting, and stylolites with subsequent tectonic activity. Knowing the timing and influence of these inversions helps to consider the current heterogeneity of the reservoir, its further potential for CO2 storage, and ways to enhance its injectivity and connections with its help. Therefore, the application of inversion-related structural changes combined with diagenetic processes like calcite dissolution facilitates the evaluation of the long-term prognosis and risk factors of CO2 storage in the chalk type of reservoirs (Bradshaw et al. , 2007; Christensen & Holloway, 2004).

7.4 Phosphatization

Chalk phosphatization (Fig. 35) is a sign that phosphorus compounds are present in the chalk sediment. The reason for this is that phosphorus-rich fluids seep through the chalk, gradually depositing phosphorus minerals inside its porous structure. Traces of phosphatization in chalk suggest the regular injection of phosphorus-rich fluids from sources like dissolved phosphorus compounds in groundwater or decomposing organic debris. For phosphatization, the environment must have a good balance between carbonate and organic carbon sedimentation rates (Jarvis, 1992), as well as a high rate of bioturbation and low sediment accumulation (Jarvis, 1992).

7.5 Silicification

In this study, we identified silicification as a common diagenetic event on the chalk samples from the Ommelanden Formation, as evidenced by the thin sections in Figures 25 and 33. What needs to be emphasized is that during the thin-section petrography analysis, it was ascertained that partly the original calcium carbonate matrix has been replaced by silica, which suggests the process of post-depositional alteration. Such substitutions are best demonstrated by the fact that the outlines of the fossils are normally preserved within the rocks that have been altered in a way that mainly darkens them in relation to the non-silicified rock.

The thin sections indicate a possible link between silicification and the impregnation of silica-bearing fluids, likely from biogenic sources such as sponge spicules and radiolarians. This type of silicification has a direct emanation from the regional setting of marine deposition that was characteristic of these organisms. The well sedimentary logs clearly show that the abundance of silica in the silicification process of the samples under study could have been provided by the shells of sponge spicules and radiolarians. As silica fills the pores, it partially alters the reservoir's properties by reducing porosity and permeability.

The observations made in the present work correlate with the descriptions of Holland (1978), who pointed to comparable phenomena in other paleontological chalk formations. Also, silica-rich water, which may result from volcanic activity or high levels of organic productivity, reveals that the depositional environment was characterized by definite geochemical circumstances that promoted

silicification. These conditions may have brought about the mobilization and precipitation of silica because of the densely silicified zones that were observed in the thin sections.

The occurrence of silicification in the Ommelanden Formation can be used to understand the paleoenvironmental conditions during deposition, which are likely to be a dynamic system influenced by biogenic influx or volcanic processes. It is not only able to provide knowledge of past environmental conditions but is also significant for evaluating the reservoir quality and the potential of CO2 storage in the formation.

7.6 Glauconite

In the detailed examination of the chalk samples that have been collected from the Ommelanden Formation, a mere 1% to 2% of glauconite has been found in thin sections from HRL_02 and HRL-04, respectively, as shown in Figure. 38. Based on the presence of glauconite, coupled with an observed abundance in bioturbation, the depositional model and diagenetic genesis of this formation are described.

Glauconite is likely to crystallize in marine environments under specific conditions where the sedimentation rates are low to medium and in slightly reducing conditions at the sediment-water interface. Such conditions enable the reduction of iron and the formation of glauconite to occur (López-Quirós, 2019). The occurrence of glauconite can therefore be used wherever it can be identified, to indicate conditions that were characterized by a slow rate of sedimentation, allowing for the formation of this mineral in the samples under consideration.

However, the presence of bioturbation in the same samples suggests an oxygenated environment and active benthos in the sediments. This implies that the depositional environment was characterized by fluctuating redox conditions. Bioturbation is evidence of periods of higher oxygen content where the benthos could, in turn, transport itself through the sediment.

The bioturbation and glauconite coexistence can only be explained by episodes of different environmental conditions. During periods of higher sea levels, the slower sedimentation rate might have allowed the formation of glauconite in localized and slightly reduced microenvironments within the sediment matrix or in less disturbed layers. Meanwhile, bioturbation could occur during more oxygenated phases, when benthic organisms were active.

The reducing and oxygenated conditions interplay complexity is reflected in the sedimentary logs and thin sections showing higher bioturbation in intervals such as lower bioturbation and glauconite mineralization. The periodic changes in sea levels influencing sedimentation rates were one of the factors behind the formation of bioturbation, and the presence of glauconite indicated a dynamic depositional environment. This is in accordance with conceptual models that relate glauconite formation to transgressive system tracts as well as high sea level regimes (Baum and Vail, 1988), while allowing for bioturbation.

7.7 Impacts of sedimentary structures and depositional environment on the flow characteristics of the chalk

In the Harlingen Gas Field, the two wells HRL 02 and HRL 04 core analyses for the Ommelanden Formation indicate the overall core is largely dominated by chalk bioturbation and mudstone to

wackestone microfacies. These cores have small differences in grain size, grade of bioturbation, and the occurrence of freely opened fractured stylolites. In HRL_02, high-intensity open stylolites were identified ranging from 1060.4 m to 1062.4 m in the uppermost part of the core, which is attributed to enhanced permeability and, as such, will be the most appropriate zone for fluid flow. The final zone of high stylolite intensity was defined at the base of the core interval, 1073.9 m to 1082.4 m, where the permeability is also increased, hence, this region is best suited for the flow of fluids and perhaps CO2 storage. These intervals are also associated with high porosity values, where plug porosity measurements were 27% at the depths of 1065 meters, 1070 meters, and 1075 meters. Higher intensity of bioturbation in the upper and basal parts of the cored interval, accompanied by increased bed-parallel stylolitization and fracturing along stylolites, are observed and are attributed to have occurred during the inversion episodes during the Upper Cretaceous and the Oligocene to Middle Miocene times. These structures greatly increase the favorable characteristics of the flow observed in the formation.

Further evidence is derived from the analysis of well logs. The gamma-ray (GR) logs of HRL_02 lying in the range of 18 API to 27 API values are also indicative of chalk formations. The interval from 1060 m to 1069 m of the upper part of the core contains low-frequency cycles of rising from low GR to high GR, probably associated with rising clay content or radioactive elements, and clean chalk is generally represented with less clay content, hence, low GR. Particularly, the presence of stylolites and fractures is well correlated to high GR readings in HRL_02 at 1062 m and 1075 m depth.

Another set of permeability measurements also points out the extent of influence that the Ommelanden Formation's sedimentary structures have on flow characteristics. The horizontal permeability values in HRL_02 range from 8 mD to 1 mD; the highest values were observed in the intervals with higher stylolite intensity. The measurements of TinyPerm 3 are less accurate but suggest that relative permeability ranges from 120 mD to 200 mD, with the highest permeability in the top 6 meters and the bottom 2 meters of the core. These observations are in correlation with the inferred zones of high stylolite intensity and porosity, pointing to the fact that these areas are more favorable for the flow of fluids, which in turn increases the possibility of CO2 storage for the reservoir.

The measured plug porosity in HRL_04 (Fig. 16) further confirms the reservoir's great potential. High porosity values, ranging from 22.7% to 33%, were measured from 10 different depths, indicating high porous zones throughout the core. Petrographical analysis from Thin Sections H, I, J, K, and L at 1052 m, 1053.5 m, 1055 m, 1057 m, and 1058 m, respectively, shows an abundance of irregular undulating patterns typical of fractures. The association of these high porosity intervals with highly fractured zones presents excellent reservoir characteristics for carbon capture and storage.

In HRL_02 microCT analysis at 1061 m depth, clear fractures are mostly horizontal with an inclined angle and seem to be more continuous laterally and not well connected. Open stylolites are observed in Thin Sections C, D, and F at 1066.9 m, 1069.6 m, and 1072.8 m, respectively. The combinations of microfractures, high porosity, and stylolite intensity, are highly effective for CO2 storage in the Ommelanden Formation.

Lastly, having incorporated the core analysis, well logs, thin section petrography, and permeability data, it is clear the Ommelanden Formation has profound flow properties for CO2 storage. Stylolites and fractures documented in the formation, especially in the bioturbated section, provide channels for fluid flow and make the formation amicable for CO2 storage. Due to its high porosity, increased permeability, and structures such as stylolites and fractures within the Ommelanden

Formation, the prospect of long-term CCS stability can be achieved through the use of various trapping mechanisms that will be elaborated on in another section.

7.8 stylolite and bioturbation effects on flow

Considering the pressure dissolution, bed parallel stylolites (BPS) are common diagenetic features in the investigated cores of the Ommelanden Formation. Core analysis in HRL_02 and HRL_04 showed that most of the stylolites are on the millimeter scale, especially when bioturbations were intense. For example, HRL_02 core sections between 1060.4 m and 1062.4 m and between 1073.9 m and 1082.4 m overlaid high stylolite seam intensity with the presence of moderate to high bioturbation. This preferential development of stylolites in bioturbated zones is due to changes in compaction and diagenesis by bioturbating organisms that increase chemical heterogeneity and pressure dissolution in localized areas.

The effects appear in the chalk formation flow characteristics, where bed-parallel stylolites and bioturbation coexist with each other. These stylolites are categorized as open stylolites when seen through micro-CT and are regarded as the primary lateral pathways for fluid movement that greatly improve permeability in intervals that have bioturbation. These open stylolites, which were formed after tectonic inversion and uplift in the Oligocene to Middle Miocene inversion, cut across bioturbated zones in such a way that the established flow paths are interconnected. For example, in HRL_02, the micro-CT images combined at 10 61. 1 m depth observed sub-horizontal microfractures linked by stylolites and bioturbation confirming the complexity of the interlocking and high permeability of the reservoir.

The petrophysical data support these observations because the intervals of high permeability of up to 10 mD are associated with an increased intensity of bioturbation and stylolites. Gamma-ray values of 18–27 API and neutron porosity logs of 750–820 PU from HRL_02, coupled with high porosity readings from core samples (up to 33%), depict that these geologic features enhance the formation's porosity and permeability rates. In the same way, at HRL_04, the readings of gamma-rays ranging from 6 to 17 gAPI and neutron porosity ranging from 22 to 26 PU correspond to higher permeable values up to 8.5 mD resulting from the increased bioturbation and open fracture zones.

One of the first to address the possibility of stylolites acting as hydrocarbon conduits was Braithwaite (1988), after examining samples from Hadeland, Norway, and Montana, USA. He concluded that stylolites may play a role in the migration of hydrocarbons from the source to the reservoir. In these systems, overpressure contributes to the stylolite's capacity to stay open and creates very permeable characteristics that enable fluids to migrate freely at high rates. This behavior was proven and demonstrated by Koehn et al. (2012) and Peacock et al. (2017), who interpret the zones of stylolites as conduits for flow, allowing fluid to move freely inside the reservoir and enhancing permeability.

7.9 Chalk Trapping Mechanisms

Open fractured chalks in the HRL wells, bioturbated, stylolitized, and dissolved by tectonic inversions, make the chalk reservoir suitable for solution or capillary trapping. For example, in HRL_02 at the various depths from 1060.4 m to 1062.4 m, and from 1073.9 m to 1082.4 m, due to very high stylolite intensity together with moderate to high bioturbation, the mechanical and chemical aspects regarding the open fracture network together with carbon may enhance these fractures by dissolution and then reprecipitation (Bonto et al., 2021). HRL_04 zone 1 from 1038 m to 1058 m of high stylolites and observed open fractures from several thin sections. These characteristics contribute to a much higher degree in increasing the reservoir's permeability and porosity, making it highly suitable for CO2 storage. Porosity in these intervals was found to be between 23% and 33%, and permeability values ranged from 0.1 mD to 40.7 mD, as established in a study to reflect the efficiency of the processes associated with the solution and capillary trapping schemes. The open fractures identified in the HRL_04 well from 1052 m to 1058 m add to the evidence pointing to the likelihood of increased fluid

connectivity, which is imperative in the provision of long-term CO2 storage. The results corroborate prior studies, in which such geologic structures enhance the capability and safety of CO2 storage and sequestration projects.

The Chalk Formation represents a potentially favorable geologic formation to store CO2, by using multiple trapping techniques to guarantee its success. Solution trapping is the primary technique where injected CO2 dissolves over time in the formation water to increase its density and, therefore, the convective mixing driven by CO2 solubility pressure (Bonto et al., 2021; Ennis-King & Paterson, 2002, 2005). In HRL_04, the interpreted dissolution of thin fractures may yield a natural example of the results of the Ommelanden chalk dissolution. The development of a similar fracture network will ensure that the injected CO2 is stored and could provide further permeability and flow connectivity. The presence of residual oil in depleted chalk fields may also increase CO2 solubility, as identified by Stewart et al. (2017).

The third and fine mechanism is proven by capillary trapping, where up to 95% of the injected CO2 can be trapped within the reservoir pores and thus have a very low probability of leakage (Krevor et al., 2015). Different authors have indicated that chalk, among other types of carbonate reservoirs, has good capillary trapping efficiency irrespective of the wettability and heterogeneity effects (Akbarabadi and Piri, 2015; Wang and Tokunaga, 2015). Also, mineral trapping ensnares CO2 through geochemical reactions, and the dissolved CO2 makes an effort to enhance the dissolution of calcite, which re-precipitates as carbonate minerals to give permanency to the storage (Zuddas & Mucci, 1994; Rosenbauer et al., 2005). Other experimental findings by Yu et al. (2023) revealed that up to 80% of the pore volume of the pure carbonate rock chalk can be sequestered by calcite precipitation.

Khather et al. (2020) also focused on the impact of the CO2-saturated brine injection, whose results showed that the injection of CO2-saturated brine led to increased permeability at the injection well site because of the dissolution of These interactions regarding pore surface chemistry and the geological models, in particular, are associated with the aforementioned comprehensive understanding needed for proper assessment of CO2 storage capacity, as underlined by Bradshaw et al. (2007). These formations, due to their capability of handling the trapping mechanisms mentioned above, and chalk's peculiar characteristics, are conducive to CO2 storage that is both injectable and inherently sequestered in the long run.

7.10 Implications of quantitative characterization on CCS in chalk in HRL

The quantitative characterization of the bioturbated chalk facies and later diagenetic processes such as stylolites and open fractures increase the permeability by a factor of at least two times, according to air permeability measurements. For instance, TinyPerm measurements in the HRL_02 well, particularly at 1064 m, 1065.5 m, 1069.5 m, and 1080 m, show a significant increase in permeability from approximately 100–120 mD in less fractured zones to 180–200 mD in zones with a high intensity of stylolites and open fractures (Figs. 12, and 15). Our study included core analyses that were obtained from the subsurface geology of HRL_02, and HRL_04, together with sedimentary logging and interpretation of wireline logs, quantitative petrography, and micro-CT image analysis. This approach allowed us to produce a representative quantitative assessment of the Ommelanden Formation in Harlingen Field, which is believed to be helpful for CCS projects in this field or similar chalk facies. The bulk rock porosity is generally from 25% to 35% (mostly micropores, with remaining macroporosity not exceeding 6%), and the horizontal and vertical permeability of HRL_02 and HRL_04 range from 1 mD to 10 mD, but the presence of the open stylolites and the vast network of fractures in the chalk reservoir make it a good candidate for CCS. Stylolites and fractures are effectively used for the formation pathways that ensure the CO2 has an easy path for injection and diffusion into the rock formation. These features enhance transmissibility, granting fluids the ability to percolate through the formation. Therefore, the injectivity in the near-borehole environment and the connectivity in the reservoir are

believed to be optimal in the presence of opened fractures, as observed in the studied cores from HRL_02 and HRL_04 wells. It is estimated that in fractured zones, the permeability of the reservoir is twice to three times greater than what is found in non-fractured zones, which means that fluid movement in fractured zones is much better and therefore there are better prospects for augmented CO2 injection and storage. This increase in permeability is most noted where there is high stylolite intensity and bioturbation: in such areas, the fractures offer a more effective path for fluid to move within the reservoir rock. Once the CO2 enters the microporous, less permeable matrix, it can mix with the formation water, which causes dissolution and then cementation as mineral trapping mechanisms. This way, extra CO2 is contained in the reservoir in the form of carbonate minerals. Furthermore, capillary trapping stores the CO2 within the pore spaces, thereby limiting leakage potentialities. This makes it possible to combine the four trapping mechanisms (i.e., structural, residual, dissolution, and mineral trapping mechanisms), guaranteeing long-term storage. Thus, the described geologic and diagenetic features contribute positively to the CCS storage capacity within the Ommelanden Formation more efficiently.

In HRL_02 well, the zones most suitable for injection are determined within the intervals of 1060.4 m to 1062.4 m and 1073.9 m to 1082.4 m. These zones have high stylolite intensity accompanied by moderate to high-grade bioturbation, which contributes to the permeability and porosity of the reservoir. The measurements for the TinyPerm within such time intervals show an uplift in permeability values from about 100–120 mD in the nonfractured areas towards about 180–200 mD in areas of high stylolite and fracture intensity. Furthermore, plug porosity measurements in these intervals are also high, measured at 27% at depths of 1065 m, 1070 m, and 1075 m.

In HRL_04 well, there are two intervals suggested for the injection of CO2. The first is the 1038 m to 1052 m interval, which records high stylolite intensity coupled with high bioturbation. These features are related to increases in permeability, and porosity, which makes this interval suitable for CO2 injections. The second interesting interval is between 1052 m and 1056 m, in which there are many highly fractured zones, especially at 1052.4 m, 1055 m, and 1056.1 m, which have resulted in permeability values within the range of 7 mD to 8.5 mD. Although there is no high permeability, the high fractures will compensate for that, along with the measured plug porosity greater than 30%. Thus, the characteristics outlined imply a good interlink between the pores along this interval, resulting in storage formation that is adequate for long-term CO2 sequestration. This way, depending on the intervals used in HRL_04, it will be possible to achieve the maximum effective injection and storage of CO2.

7.11 Depleted Oil and Gas Fields vs. Saline Aquifers

Since there is an abundance of sites suitable for CO2 storage, the determining factors for selecting storage locations will be based on the different chemical and physical aspects of the geological reservoir, trapping mechanisms, and storage challenges faced by depleted oil and gas fields or saline aquifers.

The excessive costs of drilling necessary wells, constructing the required infrastructure, and building the CO2 piping network make the use of saline aquifers for gas storage unrealizable compared to the reserves found in depleted oil and gas field infrastructure. Some disadvantages of saline formations are: water wetness leads to low injectivity; high salinity decreases CO2 solubility and diffusion, which in turn reduces solution trapping but may promote capillary trapping. Consequently, a significant quantity of CO2 injected into saline aquifers should remain in a residual, non-continuous phase. Mineral trapping might be significant over longer periods due to the chemistry of the water being influenced by the mineral phases in the reservoir (Bradshaw et al., 2007).

Depleted oil and gas fields have the advantage of known, and well-studied reservoir characterization. Proven sealing integrity, and the existence of field data and infrastructure, reduce the cost of exploration and development time. Although these fields have less storage capacity than saline aquifers, their existing infrastructure and geological knowledge lower the costs. In depleted fields, the low pressure from gaseous CO2 injection can lead to cooling effects that jeopardize the wellbore's integrity. This is not a risk in saline aquifers because the formation water has a lower ionic strength, which stops salt from precipitating. Additionally, chemical risks in depleted fields include potential asphaltene precipitation and biological activities dependent on residual oil and gas saturations (Orlic, 2016; Hettema et al., 2002).

Solution trapping is more effective in saline aquifers because of the high solubility of CO2, convection, and diffusion, but this will require multilateral wells and hence higher risks to well integrity. CO2 can also be trapped in the form of dissolved gas in the residual hydrocarbons in depleted fields, and it has a higher tendency to get trapped in small pores that are less mobile. This is because its phase is between that of water and oil. However, depleted fields have good seals with high capillary pressure to prevent the leakage of CO2, and the presence of residual oil and gas minimizes chalk reduction from the effect of carbonated water (Ennis-King and Paterson, 2005; Krevor et al., 2015).

CCS projects are known to be most prevalent in the oil and natural gas sectors because of their profitability and higher recovery rates of hydrocarbon resources. CO2 storage risks are higher in more hydrocarbon-saturated reservoirs compared to depleted ones; that is, both operational and injectivity risks could cause issues in warm reservoir fields where hydrate formation can be a problem when injecting CO2 (Bradshaw et al., 2007; Orlic, 2016).

8. Conclusion

This study of the Ommelanden Formation (Upper Cretaceous chalk) in the Harlingen Gas Field for CO2 storage, based on a comprehensive analysis using combined geological, petrophysical, petrographic, and micro-CT data, leads to the following principal conclusions:

- Carbon capture and storage is a very important approach to reducing carbon emissions and combating climate change. To achieve that, we need to study the chalk further, monitor a carbon capture and storage project taking into consideration the geomechanics, and study the reservoir for decades in order to ensure its safety and sustainability.
- The CO2 storage potential of the Ommelanden Formation is evaluated using reservoir characteristics such as facies and microfacies (bioturbated chalk, mudstone/wackestone), porosity, and permeability, and it has been demonstrated that it is highly prospective for storing CO2 with moderate (micro-)porosity values from 11% to 33% and relatively low permeability of between 0. 1 mD and 40. 7 mD. These properties, together with the presence of stylolites and bioturbation, improve the flow regime and reservoir interconnectivity in the study cases by at least two times.
- The optimal injection zones in HRL_02 are from 1060.4 m to 1062.4 m and 1073.9 m to 1082.4 m. In HRL_04, the most suitable intervals for CO2 injections are from 1038 m to 1052 m and from 1052 m to 1056 m. These primary intervals are intended for injection of CO2 because of their high porosity, permeability, stylolite, and open fracture intensity, which were chosen based on core study, petrography, and petrophysics.
- Conducted petrographic analysis of thin sections to identify microfacies; these are characterized by medium to high bioturbation, fractures by dissolution, sub-horizontal open stylolites, matrix-dominated texture, cement-reduced porosity of 1-6%, and a microporous matrix that supports the high-quality reservoir productivity for the CCS project.
- utilized micro-CT scanning techniques and analysis to identify and visualize open inclined horizontal fractures in the 3D and pore throat networks, which helped determine the effectiveness of interconnected pathways within the reservoir.
- Fractures have a tremendous impact on injectivity and connectivity. The lateral and sub-horizontal open stylolites and fractures by dissolution observed in the cores and thin sections in both HRL_02 and HRL_04 greatly increase the injection for flow pathways around the wells and contribute to the improvement of the interconnection of the reservoir. These fractures enhance the extent of CO2 migration within the reservoir and ensure better prospects for long-term storage.
- Several processes of trapping for CO2 may be successful in the Ommelanden Formation bioturbated chalk facies, such as solution trapping, capillary trapping, and mineral trapping. Formation water carbonation and subsequent mineral sequestration through calcite formation guarantee both short- and long-term sequestration stability.
- Minerals such as phosphate, glauconite, and silicification are addressed and discussed in terms of their relevance in understanding the depositional environment and their geochemical effects on the reservoir.
- Understanding the extensive description of the Ommelanden Formation in the Harlingen Field well cores can be applied as a reference for assessing other CO2 storage in these fields and other similar reservoirs. Overall, the methodologies and conclusions of this study can be used as a reference for subsequent CCS projects and reveal that project development requires the participation of multidisciplinary teams to assess reservoir characteristics and forecast storage behavior.

9. References

Abdlmutalib, A. J., Ayranci, K., Yassin, M. A., Hussaini, S. R., Abdullatif, O. A., & Humphrey, J. D. (2022). Impact of sedimentary fabrics on small-scale permeability variations within fine-grained sediments: Early Silurian Qusaiba Member, Northern Saudi Arabia. Marine and Petroleum Geology. 139, 105607.

Akbarabadi, M., Piri, M., 2015. Co-sequestration of SO2 with supercritical CO2 in carbonates: an experimental study of capillary trapping, relative permeability, and capillary pressure. Adv. Water Resour. 77, 44–56. https://doi.org/10.1016/j. advwatres.2014.08.011.

Alam, M. M., Hjuler, M. L., Christensen, H. F., & Fabricius, I. L. (2014). Petrophysical and rock-mechanics effects of CO2 injection for enhanced oil recovery: Experimental study on chalk from South Arne field, North Sea. Journal of Petroleum Science and Engineering, 122, 468-487.

Arias, P.A., N. Bellouin, E. Coppola, R.G. Jones, G. Krinner, J. Marotzke, V. Naik, M.D. Palmer, G.-K. Plattner, J. Rogelj, M. Rojas, J. Sillmann, T. Storelvmo, P.W. Thorne, B. Trewin, K. Achuta Rao, B. Adhikary, R.P. Allan, K. Armour, G. Bala, R. Barimalala, S. Berger, J.G. Canadell, C. Cassou, A. Cherchi, W. Collins, W.D. Collins, S.L. Connors, S. Corti, F. Cruz, F.J. Dentener, C. Dereczynski, A. Di Luca, A. Diongue Niang, F.J. Doblas-Reyes, A. Dosio, H. Douville, F. Engelbrecht, V. Eyring, E. Fischer, P. Forster, B. Fox-Kemper, J.S. Fuglestvedt, J.C. Fyfe, N.P. Gillett, L. Goldfarb, I. Gorodetskaya, J.M. Gutierrez, R. Hamdi, E. Hawkins, H.T. Hewitt, P. Hope, A.S. Islam, C. Jones, D.S. Kaufman, R.E. Kopp, Y. Kosaka, J. Kossin, S. Krakovska, J.-Y. Lee, J. Li, T. Mauritsen, T.K. Maycock, M. Meinshausen, S.-K. Min, P.M.S. Monteiro, T. Ngo-Duc, F. Otto, I. Pinto, A. Pirani, K. Raghavan, R. Ranasinghe, A.C. Ruane, L. Ruiz, J.-B. Sallée, B.H. Samset, S. Sathyendranath, S.I. Seneviratne, A.A. Sörensson, S. Szopa, I. Takayabu, A.-M. Tréguier, B. van den Hurk, R. Vautard, K. von Schuckmann, S. Zaehle, X. Zhang, and K. Zickfeld, 2021: Technical Summary. In Climate Change 2021: The Physical Science Basis. Contribution of Working Group I to the Sixth Assessment Report of the Intergovernmental Panel on Climate Change [Masson-Delmotte, V., P. Zhai, A. Pirani, S.L. Connors, C. Péan, S. Berger, N. Caud, Y. Chen, L. Goldfarb, M.I. Gomis, M. Huang, K. Leitzell, E. Lonnoy, J.B.R. Matthews, T.K. Maycock, T. Waterfield, O. Yelekçi, R. Yu, and B. Zhou (eds.)]. Cambridge University Press, Cambridge, United Kingdom and New York, NY, USA, pp. 33−144. doi:10.1017/9781009157896.002.

Bachu, S. (2008). CO2 storage in geological media: Role, means, status, and barriers to deployment. Progress in Energy and Combustion Science, 34(2), 254-273. https://doi.org/10.1016/j.pecs.2007.10.001.

Baniak, G. M., La Croix, A. D., & Gingras, M. K. (2022). Recent advancements in characterizing permeability and porosity distributions in bioturbated flow media. Earth-Science Reviews, 232, 104162. https://doi.org/10.1016/j.earscirev.2022.104162.

Baum, G. R., & Vail, P. R. (1988). Sequence stratigraphic concepts applied to Paleogene outcrops, Gulf and Atlantic basins.

Bradshaw, J., Bachu, S., Bonijoly, D., Burruss, R., Holloway, S., Christensen, N. P., & Mathiassen, O. M. (2007). CO2 storage capacity estimation: Issues and development of standards. International Journal of Greenhouse Gas Control, 1(1), 62-68. https://doi.org/10.1016/S1750-5836(07)00027-8.

Braithwaite, C. J. R. (1989). Stylolites as open fluid conduits. Marine and Petroleum Geology, 6(1), 93-96.
Bromley, R. G. (1996). Trace fossils. Biology, taphonomy and applications (p. 361). Chapman & Hall.
Butts, S. H. (2014). Silicification. The Paleontological Society Papers, 20, 15–34. https://doi.org/10.1017/S1089332600002783.

Cappuccio, F., Toy, V. G., Mills, S., & Adam, L. (2020). Three-dimensional separation and characterization of fractures in X-ray computed tomographic images of rocks. Frontiers in Earth Science, 8, 529263.

Carbon Monitor Organization. (2023). Carbon Monitor. Retrieved from [https://carbonmonitor.org/].

Christensen, N. P., & Holloway, S. (2004). Assessing European potential for geological storage of CO2 from fossil fuel combustion. Summary report for GESTCO (No. ENK6-Ct-1999–00010). European Union Fifth Framework Programme for Research & Development.

De Jager, J. (2003). Inverted basins in the Netherlands, similarities and differences. Netherlands Journal of Geosciences, 82(4), 339-349.

Wong, T. E., Batjes, D. A. J., & Jager, J. D. (2007). Geological development. Amsterdam, Royal Netherlands Academy of Arts and Sciences.

Ennis-King, J., & Paterson, L. (2002). Engineering aspects of geological sequestration of carbon dioxide. In SPE Asia Pacific Oil and Gas Conference and Exhibition (p. 13). Society of Petroleum Engineers. https://doi.org/10.2118/77809-MS.

Ennis-King, J. P., & Paterson, L. (2005). Role of convective mixing in the long-term storage of carbon dioxide in deep saline formations. SPE Journal, 10, 349–356. https://doi.org/10.2118/84344-PA
Esmerode, E. V., & Surlyk, F. (2009). Origin of channel systems in the Upper Cretaceous Chalk Group of the Paris Basin. Marine and Petroleum Geology, 26, 1338–1349.

Fabricius, I. L. (2000). Interpretation of burial history and rebound from loading experiments and the occurrence of microstylolites in the mixed sediments of the Caribbean Sites 999 and 1001. Proceedings of the Ocean Drilling Program, Scientific Results, 165, 177-190.

Fabricius, I. L. (2001). Compaction of microfossil and clay-rich chalk sediments. Physics and Chemistry of the Earth, 26, 59-62.
Friesen, O. J., Dashtgard, S. E., Miller, J., Schmitt, L., & Baldwin, C. (2017). Permeability heterogeneity in bioturbated sediments and implications for waterflooding of tight-oil reservoirs, Cardium Formation, Pembina Field, Alberta, Canada. Marine and Petroleum Geology, 82, 371–387.
Ghoshal, P., Kim, M. C., & Cardoso, S. S. (2017). Reactive–convective dissolution in a porous medium: the storage of carbon dioxide in saline aquifers. Physical Chemistry Chemical Physics, 19(1), 644-655..

Haq, B. U. (1991). Sequence stratigraphy, sea-level change, and significance for the deep sea. Sedimentation, Tectonics and Eustasy: Sea-Level Changes at Active Margins, 1-39.

Jarvis, I. (1992). Sedimentology, geochemistry and origin of phosphatic chalks: the Upper Cretaceous deposits of NW Europe. Sedimentology, 39(1), 55-97.
Jones, M.E., Bedford, J. & Clayton, C.J. (1984). On natural deformation mechanisms in the chalk. Journal of Geological Society (London) 141, 675-683.

Keeling, C. D. (2021). Atmospheric CO2 concentration. Retrieved from [https://scripps.ucsd.edu/programs/keelingcurve/]

Khather, M., Saeedi, A., Myers, M. B., & Giwelli, A. (2020). Effects of CO 2-Saturated Brine on the Injectivity and Integrity of Chalk Reservoirs. Transport in Porous Media, 135, 735-751.

Koehn, D., Ebner, M., Renard, F., Toussaint, R., & Passchier, C. W. (2012). Modelling of stylolite geometries and stress scaling. Earth and Planetary Science Letters, 341, 104-113.

Krevor, S., Blunt, M.J., Benson, S.M., Pentland, C.H., Reynolds, C., Al-Menhali, A., Niu, B. (2015). Capillary trapping for geologic carbon dioxide storage – From pore scale physics to field scale implications. International Journal of Greenhouse Gas Control, Special Issue commemorating the 10th year anniversary of the publication of the Intergovernmental Panel on Climate Change Special Report on CO2 Capture and Storage, 40, pp. 221–237. https://doi.org/10.1016/j.ijggc.2015.04.006.

La Croix, A. D., Gingras, M. K., Dashtgard, S. E., & Pemberton, S. G. (2012). Computer modeling bioturbation: The creation of porous and permeable fluid-flow pathways. AAPG Bulletin, 96(3), 545–556.

Liu, Y., Hou, M., Yang, G., Han, B., 2011. Solubility of CO2 in aqueous solutions of NaCl, KCl, CaCl2 and their mixed salts at different temperatures and pressures. J. Supercrit. Fluids 56, 125–129. https://doi.org/10.1016/j.supflu.2010.12.003.

López-Quirós, A., Escutia, C., Sánchez-Navas, A., Nieto, F., Garcia-Casco, A., Martín-Algarra, A., ... & Salabarnada, A. (2019). Glaucony authigenesis, maturity and alteration in the Weddell Sea: An indicator of paleoenvironmental conditions before the onset of Antarctic glaciation. Scientific reports, 9(1), 13580.

McKinney, F.K. & Hageman, S.J. (2006). Paleozoic to modern marine ecological shift displayed in the northern Adriatic Sea. Geology 34, 881–884, http://dx.doi.org/10.1130/G22707.1

McRae, S. G. (1972). Glauconite. Earth-Science Reviews, 8(4), 397-440.

Mortimore, R. (2011). A chalk revolution: what have we done to the Chalk of England? Proceedings of the Geologists' Association, 122(2), 232-297.

Olsen, D. (2010, June). CO2 IOR on North Sea Chalk: laboratory experiments at reservoir conditions. In SPE EUROPEC/EAGE Annual Conference and Exhibition. OnePetro.

Olsen, D. (2011, May). CO2 EOR production properties of chalk. In SPE EUROPEC/EAGE annual conference and exhibition. OnePetro.

Orlic, B. (2016). Geomechanical effects of CO2 storage in depleted gas reservoirs in the Netherlands: Inferences from feasibility studies and comparison with aquifer storage. Journal of Rock Mechanics and Geotechnical Engineering, 8(6), 846-859.

Peacock, D. C. P., Korneva, I., Nixon, C. W., & Rotevatn, A. (2017). Changes of scaling relationships in an evolving population: the example of “sedimentary” stylolites. Journal of Structural Geology, 96, 118-133.

Qi, Y., Wang, M., Zheng, W., & Li, D. (2012). Calcite cements in burrows and their influence on reservoir property of the Donghe Sandstone, Tarim Basin, China. Journal of Earth Science, 23(2), 129–141.

Roduit, N. JMicroVision: Image analysis toolbox for measuring and quantifying components of high-definition images. Version 1.3.1. https://jmicrovision.github.io

Rosenbauer, R.J., Koksalan, T., Palandri, J.L. (2005). Experimental investigation of CO2–brine–rock interactions at elevated temperature and pressure: Implications for CO2 sequestration in deep-saline aquifers. Fuel Process. Technol. Carbon Dioxide Capture Sequest. 86, 1581–1597. https://doi.org/10.1016/j.fuproc.2005.01.011.

Salih, M., Reijmer, J. J. G., El Husseiny, A., Bashri, M., Eltom, H., Mukainah, H. A., & Kaminski, M. A. (2021). Controlling factors on petrophysical and acoustic properties of bioturbated carbonates: (Upper Jurassic, Central Saudi Arabia). Applied Sciences, 11(11), 5019.

Stewart, R. J., Johnson, G., Haszeldine, S., Olden, P., Mackay, E., Mayer, B., & Shevalier, M. (2017). Security of storage in carbon dioxide enhanced oil recovery. Energy Procedia, 114, 3870–3878. https://doi.org/10.1016/j.egypro.2017.03.1519

Tonkin, N. S., McIlroy, D., Meyer, R., & Moore-Turpin, A. (2010). Bioturbation influence on reservoir quality: A case study from the Cretaceous Ben Nevis Formation, Jeanne'dArc Basin, offshore Newfoundland, Canada. AAPG Bulletin, 94(7), 1059–1078.

United Nations Framework Convention on Climate Change. (2015). Paris Agreement. Retrieved from [https://unfccc.int/process-and-meetings/the-paris-agreement]

van der Molen, A. (2004). "Sedimentary development, seismic stratigraphy and burial compaction of the Chalk Group in the Netherlands North Sea area." Thesis.

van Wingerden, E. (2016). Chalk facies and its petrophysical expression from core and wireline data, north sea basin, the netherlands. Thesis Report, EBN.

Vangkilde-Pedersen, T., Anthonsen, K. L., Smith, N., Kirk, K., van der Meer, B., Le Gallo, Y., ... & Christensen, N. P. (2009). Assessing European capacity for geological storage of carbon dioxide–the EU GeoCapacity project. Energy Procedia, 1(1), 2663-2670.

Wang, S., & Tokunaga, T. K. (2015). Capillary pressure–saturation relations for supercritical CO2 and brine in limestone/dolomite sands: Implications for geologic carbon sequestration in carbonate reservoirs. Environmental science & technology, 49(12), 7208-7217.

Yang, Y., Hakim, S. S., Bruns, S., Rogowska, M., Boehnert, S., Hammel, J. U., ... & Sørensen, H. O. (2018). Direct observation of coupled geochemical and geomechanical impacts on chalk microstructure evolution under elevated CO2 pressure. ACS Earth and Space Chemistry, 2(6), 618-633.

Yu, T., Gholami, R., Raza, A., Vorland, K. A. N., & Mahmoud, M. (2023). CO2 storage in chalks: What are we afraid of?. International Journal of Greenhouse Gas Control, 123, 103832.

Zuddas, P., & Mucci, A. (1994). Kinetics of calcite precipitation from seawater: I. A classical chemical kinetics description for strong electrolyte solutions. Geochimica et Cosmochimica Acta, 58(20), 4353-4362.